crystals

MDPI

Article

Synthesis, Antimicrobial and Anti-Inflammatory Activity of a Novel Styrylquinolinium Iodide Bearing a Naphthalene Moiety

Stoyan Zagorchev [1], Mina Todorova [1,*], Mina Pencheva [2], Rumyana Bakalska [1], Tsonko Kolev [3], Emiliya Cherneva [4,5], Mehran Feizi-Dehnayebi [6], Seyedsobhan Seyedhoseyni [7], Yulian Tumbarski [8], Paraskev Nedialkov [9], Francisco Alonso [10] and Stoyanka Nikolova [1,*]

1 Department of Organic Chemistry, Faculty of Chemistry, The University of Plovdiv "Paisii Hilendarski", Str., 4000 Plovdiv, Bulgaria; bakalska@uni-plovdiv.bg (R.B.)
2 Department of Medical Physics and Biophysics, Faculty of Pharmacy, Medical University of Plovdiv, 4002 Plovdiv, Bulgaria; mina.pencheva@mu-plovdiv.bg
3 Institute of Molecular Biology "Acad. Roumen Tsanev", Bulgarian Academy of Sciences, 1113 Sofia, Bulgaria; tskolev@bio21.bas.bg
4 Department of Chemistry, Faculty of Pharmacy, Medical University of Sofia, 2 Dunav Str., 1000 Sofia, Bulgaria; cherneva@pharmfac.mu-sofia.bg
5 Institute of Organic Chemistry with Centre of Phytochemistry, Bulgarian Academy of Sciences, 1113 Sofia, Bulgaria
6 Department of Basic Pharmaceutical Sciences, Faculty of Pharmacy, Suleyman Demirel University, 32260 Isparta, Turkey; m.feizi@alzahra.ac.ir
7 Department of Chemistry, Faculty of Science, Karaj Branch, Islamic Azad University, Karaj P.O. Box 31485-313, Iran; so.hoseyni1@gmail.com
8 Department of Microbiology and Biotechnology, Technological Faculty, University of Food Technologies, 4002 Plovdiv, Bulgaria
9 Department of Pharmacognosy, Faculty of Pharmacy, Medical University of Sofia, 1000 Sofia, Bulgaria; pnedialkov@pharmfac.mu-sofia.bg
10 Instituto de Síntesis Orgánica (ISO) and Departamento de Química Orgánica, Facultad de Ciencias, Universidad de Alicante, 03080 Alicante, Spain; falonso@ua.es
* Correspondence: minatodorova@uni-plovdiv.bg (M.T.); tanya@uni-plovdiv.bg (S.N.)

Abstract

The use of styrylium dyes as organic nonlinear optical materials in many photonics domains has been the subject of research for decades. It has been noted that over time, research has also looked into the biological activity of styrylium dyes, namely their antibacterial effects, as well as attempts to establish links between structure and property by choosing particular structural pieces. These investigations' scope is still very limited. Therefore, our main goal was to synthesize a styrylium compound with antimicrobial potential. A novel styrylquinolinium compound (**D**) was synthesized using Knoevenagel condensation. Spectroscopic techniques, including IR, 1D and 2D NMR (COSY, HSQC, and HMBC), HRMS spectra, and X-ray analysis, were used to confirm its structure. The antimicrobial and anti-inflammatory activity of the compound was assessed. The compound was found to have very good antimicrobial activity against five Gram-positive strains, three Gram-negative strains, and fungi. The most pronounced effect of the compound was against *Escherichia coli* and *Pseudomonas aeruginosa*. The compound's anti-inflammatory activity was evaluated through its ex vivo immunohistochemistry. DFT calculations, such as geometry optimization, Molecular Electrostatic Potential (MEP), HOMO–LUMO, reactivity parameters and molecular docking simulation were applied to investigate the electronic features of the compound and confirm the biological activity. The compound (**D**) demonstrated a promising antibacterial and immunomodulatory profile. Its ability to induce IL-1β and at the same time moderately reduce NOS3 can be considered as a controlled adaptation

Check for updates

Academic Editor: Emilio Parisini

Received: 20 January 2026
Revised: 2 February 2026
Accepted: 3 February 2026
Published: 5 February 2026

Copyright: © 2026 by the authors. Licensee MDPI, Basel, Switzerland. This article is an open access article distributed under the terms and conditions of the Creative Commons Attribution (CC BY) license.

of the immune response, especially in cases requiring local immune activation. Docking simulation revealed that (**D**) binds effectively to the active site of the bacterial protein, supporting the experimental findings of the compound's antibacterial activity.

Keywords: synthesis; styrylquinolinium salts; crystal structure; antimicrobial; anti-inflammatory

1. Introduction

The World Health Organization (WHO) estimates that gastrointestinal disorders brought on by different bacterial and viral infections account for around a quarter of a million deaths per year [1]. Both the food sector and the hospital setting employ a range of antimicrobial treatments, including disinfectants and antibiotics, to manage and prevent microbial infections. Many bacterial pathogens have developed resistance to certain antibacterial drugs as a result of the extensive use and abuse of antibiotics [2]. Multidrug-resistant microorganisms are seen as a major threat to world health. These pathogens are bacteria, viruses, fungi, or parasites that have developed resistance to conventional therapy as a result of improper antibiotic use, eating unclean food, inadequate infection prevention, poor sanitation, etc. Prolonged illness, high healthcare expenses, disease progression, and an increased risk of death are caused by the formation of these novel resistance mechanisms and the ineffectiveness of medications and treatments against microbial infections [3].

Bacteria that aggregate, adhere to surfaces, and are encased in an extracellular polymeric matrix form biofilms. The local environment of a biofilm shields persister cells from the immune system [4]. Bacterial biofilms can form on any surface, including hospital water distribution systems and medical implants [5]. A notable pathogen, *P. aeruginosa*, exemplifies a bacterium that can be extremely difficult to eliminate and lead to treatment complications, especially within a biofilm. In the present day, antibiotic resistance is a long-lasting issue globally, and various strong medications have failed to manage diseases.

Pseudomonas aeruginosa is an important Gram-negative aerobic bacillus to consider in the differential diagnosis of various infections, such as chronic obstructive pulmonary disease, cystic fibrosis, cancer, traumas, burns, sepsis, and pneumonia [6–10]. In clinical environments, it represents a considerable challenge because of its intricate antibiotic resistance mechanisms, ability to form biofilms, and potential for causing lasting infections in humans and animals alike [11,12]. *Pseudomonas aeruginosa* has numerous mechanisms of antibiotic resistance and a range of virulence factors, which explain the wide variety of infections it causes and the growing difficulties in treating the resulting antimicrobial resistance [13,14]. Several mechanisms have been recognized for *Pseudomonas* antibiotic resistance, such as intrinsic antibiotic resistance, efflux systems, and enzymes that inactivate antibiotics [15,16]. Infections caused by *P. aeruginosa* are believed to be linked to more than 300,000 deaths each year and rank at the top of the WHO's priority list for research and development of new antibiotics [17,18]. Significantly, *P. aeruginosa* is among the most significant pathogens, which include *Enterococcus faecium*, *Staphylococcus aureus*, *Klebsiella pneumoniae*, *Acinetobacter baumannii*, and *Enterobacter*. According to the WHO, carbapenem-resistant *P. aeruginosa* is classified as a "critical" group of pathogens that urgently requires new antibiotics in clinical settings [19].

Therefore, more efficient research into long-acting and broad-spectrum antibacterial medicines for biological applications is required to address this issue.

Quaternary ammonium compounds are among the most widely utilized antibacterial substances. Although the precise antibacterial mechanism of quaternary ammonium compounds is not entirely understood, it is thought that either physical damage of the cell

wall or suppression of cell wall processes is the main mode of action [20]. Numerous elements, including molecular weight, N-alkyl chain length, and counterion type, contribute to quaternary ammonium compounds' antibacterial activity [21].

The length of the hydrophobic aliphatic chain affects the compound's action [22]. The quaternary ammonium compounds are more likely to pierce the hydrophobic bacterial membrane. The strength of the cationic moieties and the length of the alkyl chains mostly control the amphiphilic equilibrium between hydrophobicity and hydrophilicity. The degree of penetration into the bacterial membrane is altered by a shift in the amphiphilic balance. The quaternary ammonium compound's molecular weight and solubility are influenced by the type of counterion [23].

Stilbene derivatives are among the quaternary ammonium compounds that have certain pharmacological characteristics and biological functions in plant defense [24]. Styrylpyridinium and styrylquinolinium dyes have been shown to have antimicrobial properties. The type of anion and the type of electron-donating group—dimethylamino, ethoxy, hydroxy, π-conjugated bridge—and electron-withdrawing group are thought to have an impact on this biological activity. The positively charged pyridinium and quinolinium cores, seen in Figure 1 [25], are thought to be the primary structural components linked to these compounds' activity.

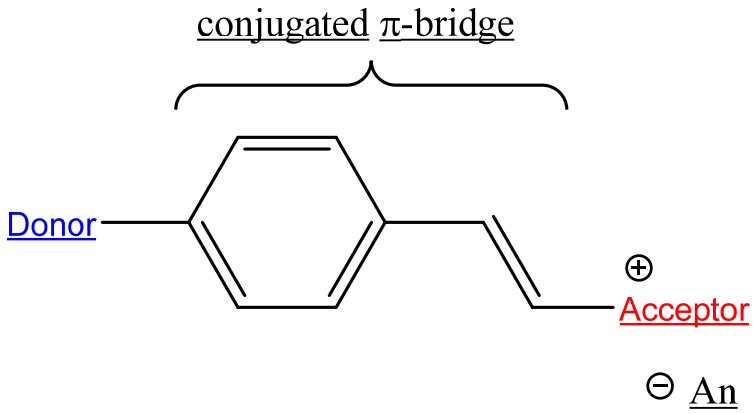


Figure 1. Main structural components influencing antimicrobial properties.

Styrylium compounds, specifically styrylquinolinium salts, are well-known compounds that have been found to possess antimicrobial activity against Gram-positive and Gram-negative bacteria, as well as against fungi and yeasts [25,26].

To this day, interest in these compounds is still high due to their wide range of applications. Exceptionally strong nonlinear optical and electro-optical effects distinguish these compounds [27]. These molecules are attractive as potential nontoxic biological staining agents that are easy to synthesize, possess photostability, and have a high fluorescence quantum yield in the presence of nucleic acids [28,29]. Bioimaging of the plasma membrane of plant and animal cells, including neurons, has been successfully performed by fluorescent staining with styrylium compounds [30]. Styrylium salts have been proposed as a fluorescent probe for early Alzheimer's disease detection, due to their demonstrated propensity to generate tau aggregates in vitro and in living cells [31]. Furthermore, these compounds have been found to selectively stain mitochondria in living cells [32,33]. Recently, studies have also been done on their biological activity and they have been found to possess antimicrobial activity against both Gram-positive and Gram-negative bacteria, as well as against fungi and yeasts [26,34]. Their donor–π-bridge–acceptor structure suggests they have these properties as electron mediators in bioelectrochemical systems [34]. The potential of styrylquinolinium is still unexplored, and therefore it makes sense to make new

modifications to its structure, as well as to investigate its structure–activity relationship. Therefore, our main goal was to synthesize a styrylium compound with antimicrobial potential targeting *P. aeruginosa*.

In recent years, computational chemistry has become an indispensable tool in modern drug design and molecular characterization, offering detailed insights into molecular geometry, reactivity, and interaction mechanisms that are often inaccessible through experimental methods alone. Density functional theory (DFT) calculations provide precise information on molecular stability, electronic distribution, and reactive sites, enabling the prediction of chemical behavior and structure–activity relationships [35]. Additionally, molecular docking simulations allow for a predictive understanding of ligand–target interactions at the molecular level, thereby supporting the experimental evaluation of biological activity. Recent studies have used these computational methods to explore the electronic behavior, structural analysis, and biological activity of compounds [36,37]. In our study, we employed DFT and molecular docking analyses to comprehensively investigate the structural, electronic, and binding characteristics of the newly synthesized compound **D**. These computational techniques were essential for correlating structural parameters with biological properties and for validating experimental findings with theoretical data. The novelty of our approach lies in the integrated use of DFT (including Molecular Electrostatic Potential (MEP), HOMO–LUMO, and reactivity descriptors) and docking models to understand both chemical reactivity and biological affinity, particularly targeting the *Escherichia coli* protein (PDB ID: 2VF5). This dual strategy enhances the predictive accuracy of bioactivity assessments and provides a rational basis for future molecular modifications.

2. Materials and Methods

2.1. Spectroscopic Methods

2.1.1. IR-Spectra

On a VERTEX 70 FT-IR spectrometer (Bruker Optics, Billerica, MA, USA) in KBr pellets, the infrared spectrum of styrylquinolinium (**D**) was recorded in the range of 4000 to 400 cm^{-1}, with a resolution of 2 cm^{-1} and 26 scans.

2.1.2. NMR-Spectra

NMR spectra of (**D**) were taken on a Bruker Avance (Bruker BioSpin GmbH, Rheinstetten, Germany) (500 MHz). Two-dimensional techniques—homonuclear proton–proton correlation (COSY), and heteronuclear proton–carbon correlation through one bond (HSQC) and through two–three bonds (HMBC)—were also applied. All acquisitions employed DMSO-d6 as the deuterated solvent. Coupling constants, or J-values, are given in Hz, and chemical shifts are represented in ppm (δ).

2.1.3. HR-ESI-MS-Spectra

A high-resolution electrospray ionization mass spectrum (HR-ESI-MS) was acquired in positive mode on a Q Exactive Plus (ThermoFisher Scientific, Inc., Bremen, Germany) mass spectrometer, equipped with a heated HESI-II source. Aliquots of 1 µL of the solutions of the samples (ca. 20 µg mL^{-1}) were introduced into the mass spectrometer via the LC system Thermo Scientific Dionex Ultimate 3000 RSLC (Thermo Fisher Scientific, Germering, Germany), consisting of a 6-channel SRD-3600 degasser, HPG-3400RS high-pressure gradient pump, WPS-3000TRS autosampler, and TCC-3000RS column compartment equipped with a narrow-bore Hypersil GOLD™ C18 (2.1 × 50 mm, 1.9 µm) column. Each chromatographic run was carried out isocratically with a mobile phase consisting of water/acetonitrile/methanol/acetic acid (25:50:25:0.2). Xcalibur (Thermo Fisher Scientific, Waltham, MA, USA) ver. 4.0 was used for data acquisition and processing.

2.1.4. Crystal Structure

A single crystal of 2511285 (TN-1) was analyzed by X-ray diffraction, and a summary of the crystallographic data and the structure refinement parameters is reported in Table 1. Crystallographic data were collected at 298 K using a Bruker D8 Venture diffractometer with a Photon III C14 detector and Cu-Kα radiation (λ = 1.54178 Å) generated by an Incoatec microfocus diamond II source (Incoatec GmbH, Geesthacht, Germany).

Table 1. Crystal data and structure refinement of (**D**).

Empirical formula	C_{31} H_{37} I N_2
Formula weight	564.52
Temperature	298.90 K
Wavelength	1.54178 Å
Crystal system	Monoclinic
Space group	P 1 $2_{1/c}$ 1
Unit cell dimensions	a = 19.776(2) Å, α = 90° b = 7.6398(8) Å, β = 98.394(3)° c = 18.869(2) Å, γ = 90°
Volume	2820.3(5) $Å^3$
Z	4
Density (calculated)	1.330 Mg/m^3
Absorption coefficient	9.057 mm^{-1}
F(000)	1160
Crystal size	0.211 × 0.128 × 0.1 mm^3
Theta range for data collection	4.520 to 68.308°
Index ranges	−23 <= h <= 23, −9 <= k <= 9, −20 <= l <= 22
Reflections collected	70250
Independent reflections	5146 [R(int) = 0.0428]
Completeness to theta = 67.679°	99.5%
Absorption correction	Semi-empirical from equivalents
Max. and min. transmission	0.7531 and 0.3529
Refinement method	Full-matrix least-squares on F^2
Data/restraints/parameters	5146/0/305
Goodness-of-fit on F^2	1.072
Final R indices [I > 2sigma(I)]	R_1 = 0.0346, wR_2 = 0.0991
R indices (all data)	R_1 = 0.0352, wR_2 = 0.1001
Extinction coefficient	0.00087(12)
Largest diff. peak and hole	1.293 and −0.610 e·$Å^{-3}$

The software APEX6- Version:2024.9-0 (Bruker AXS Inc., 2024) [38] was used for collecting frames of data, indexing reflections, and determination of lattice parameters, SAINT Version 8.41 (Bruker AXS Inc., 2016) [39] for integration of intensity of reflections, and SADABS Version 2016/2 [40] for scaling and empirical absorption correction. The structure was solved by a dual-space algorithm using the program SHELXT Version 2018/2 [41]. All non-hydrogen atoms were refined with anisotropic displacement parameters by full-matrix least-squares calculations on F^2 using the program SHELXL Version 2019 [42] with OLEX2 1.5 [43]. Hydrogen atoms were inserted at calculated positions and constrained with isotropic displacement. Drawings were produced with MERCURY: ***visualization and analysis of crystal structures*** [44].

2.1.5. DFT Perspective

The compound **D** underwent geometry optimization using DFT with the B3LYP functional. All calculations were carried out in the gas phase utilizing the Gaussian 09W software suite [45], and molecular visualizations were generated using GaussView

6.0. A 6-311g (d,p) basis set was applied to every atom in the structure. To verify that the optimized geometries represented actual energy minima, frequency analysis was conducted simultaneously with the optimization process, using the same theoretical parameters. Following optimization, further analysis was performed to evaluate the MEP distribution, HOMO–LUMO orbitals, and quantum chemical reactivity descriptors. The UV-Vis spectrum of the compound was computed using time-dependent density functional theory (TD-DFT) with the CPCM solvation model, employing ethanol as the solvent.

2.1.6. Molecular Docking Modeling

The antibacterial potential of pharmacological compound (**D**) was evaluated through in silico molecular docking studies. For this purpose, AutoDock 4.2 alongside AutoDock Tools 1.5.6 [46] was employed to identify the most favorable binding orientation between the synthesized molecule and specific target macromolecules. The crystal structure of the *Escherichia coli* protein (PDB ID: 2VF5) was retrieved from the Protein Data Bank (PDB). Prior to the docking procedure, the protein structure was preprocessed by removing water molecules and irrelevant ligands. Kollman charges and hydrogen atoms were subsequently added to prepare the structure for simulation. A grid box measuring 100 × 100 × 100 points with a spacing of 0.375 Å was centered on the 2VF5 protein to define the search area. Docking simulations were executed using the Lamarckian Genetic Algorithm (LGA) under default settings. The optimal binding conformation obtained from the simulation output was further analyzed using Discovery Studio Visualizer 4.1.

2.2. Ex Vivo Anti-Inflammatory Activity

2.2.1. Immunohistochemical Analysis

Immunohistochemical testing was performed on formalin-fixed, paraffin-embedded 5 µm sections. The sections were incubated for a minimum of 20 min at 90 °C and afterward deparaffinized. Immunohistochemically, both lungs were examined with IL-1β and NOS3 primary antibodies (Elabscience Biotechnology Inc., Houston, TX, USA). Immunohistochemical (IHC) staining was performed with Autostainer Link 48 (Dako, Agilent Technologies Inc., Glostrup, Denmark). We use optimized reagents for Autostainer Link 48 with FLEX Ready-to-Use Antibodies and EnVision FLEX Visualization Systems.

2.2.2. Histology and Immunohistochemistry

The morphometric analysis involved gastric tissue slices 5 µm in thickness, obtained from the circular and longitudinal layer of SM cells, as well as in the myenteric plexus of the stomach. The intensity of the immune reaction in the stomach was measured in arbitrary units (AU) on the slices immunostained for IL-1β and NOS3. The measurements were performed using DP–Soft ver. 3.2 software, Olympus, Japan. A minimum of 50 points was measured in the stomach at magnification ×400.

2.3. Antimicrobial Activity

The antimicrobial activity of compound (**D**) was determined by the agar well diffusion method [47].

The minimum inhibitory concentration (MIC) is determined by the two-fold serial dilution method. The test extract is diluted twice in methanol in the range from 100 mg/mL to 0.05 mg/mL. The test microorganisms are pre-inoculated in the respective agar culture media in Petri dishes, and after the agar has solidified, six wells are punched. Samples from each dilution are added in an amount of 60 µL to the wells, after which the Petri dishes are incubated under the appropriate conditions, depending on the type of test microorganism. The MIC value is taken as the lowest concentration of the extract that completely inhibits the growth of each test microorganism around the agar well.

2.4. Synthetic Procedure

All reagents were purchased from Merck (Merck KGaA, Darmstadt, Germany).

2.4.1. Lepidinium Octyl Iodide (**B**)

In a 20 mL toluene solution containing 2.15 g (0.015 mol) of lepidine, 3.60 g (0.015 mol) of n-octyl iodide was added dropwise. After 13 h of boiling, the quaternary salt was produced. The reaction was monitored by TLC with C_6H_6:CH_3OH (9:1, *v*/*v*) or C_6H_6:CH_3OH (7.5:2.5, *v*/*v*) mixture as the eluent. The resulting dark green oil was filtered. The reaction mixture was subjected to vacuum distillation to remove the unreacted lepidin. It was kept cold in a refrigerated room. Column chromatography was utilized to purify lepidinium octyl iodide, with eluent benzene: methanol (9:1). Cerium sulfate was used to visualize the product.

2.4.2. 4-{(E)-2-[4-(Dimethylamino)naphthalen-1-yl]ethenyl}-1-octylquinolinium iodide (**D**)

In a 100 mL round flask, lepidinium octyl iodide, 0.54 g (0.0014 mol), and 4-*N*,*N*-dimethylaminonaphthaldehyde, 0.28 g (0.0014 mol), were added in 20 mL dry benzene. Piperidine (0.012 g; 0.00014 mol) and glacial acetic acid (0.07 g; 0.00028 mol) were added to the mixture. The reaction mixture was boiled with a reflux condenser and calcium chloride drying tube on top of the condenser. The wine-red crystals were filtered off after 28 h, cleaned with benzene, and allowed to dry at room temperature. TLC was used for monitoring the progress of the reaction. Propanol:formic acid (8:2, *v*/*v*) or petroleum ether: diethyl ether (2:1, *v*/*v*) were used to elute the product, and UV light or I_2-vapor was used to visualize it.

4-{(E)-2-[4-(dimethylamino)naphthalen-1-yl]ethenyl}-1-octylquinolinium iodide-IR (KBr) υ/cm^{-1}: 3061; 3037; 2961; 2932; 2925; 2854; 2824; 2775; 1602; 1596; 1558; 1532; 1514; 1467; 1456; 1452; 1404; 1342; 1331; 1284; 1238; 1224; 1170; 1167; 1142; 1096; 1060; 1045; 976; 974; 970; 950; 913; 876; 836; 777; 765; 730; 561; 485.

^{1}H NMR (500 MHz, DMSO): δ 9.36 (d, *J* = 6.6 Hz, 1H, H2), 9.09 (d, *J* = 8.9 Hz, 1H, H5), 8.96 (d, *J* = 15.5 Hz, 1H, H_β), 8.80 (d, *J* = 6.9 Hz, 1H, H3), 8.65 (d, *J* = 8.5 Hz, 1H, H5″), 8.54 (d, *J* = 8.9 Hz, 1H, H8), 8.45 (d, *J* = 8.2 Hz, 1H, H2′), 8.32 (d, *J* = 15.8 Hz, 1H, H_α), 8.25 (t, *J* = 8.7 Hz, 1H, H7), 8.21 (d, *J* = 8.9, 1.1 Hz, 1H, H8′), 8.03 (t, *J* = 7.4 Hz, 1H, H6), 7.68 (t, *J* = 7.6 Hz, 1H, H7′), 7.61 (t, 1H, H6′), 7.21 (d, *J* = 8.2 Hz, 1H, H3′), 4.98 (t, *J* = 7.6 Hz, 2H, N^+CH_2, 1″), 2.97 (s, 6H, $N(CH_3)_2$), 1.96 (m, 2H, CH_2, 2″), 1.41 (m, 2H, CH_2, 3″), 1.32 (m, *J* = 14.9, 6.7 Hz, 2H, CH_2, 4″), 1.26 (m, 6H, CH_2, 5″; CH_2, 6″; CH_2, 7″), 0.86 (t, *J* = 6.9 Hz, 3H, CH_3, 8″).

^{13}C NMR (126 MHz, DMSO) δ 154.26 (C4′), 153.23 (C4), 147.45 (C2), 139.95 (C_β), 138.31 (C8a), 135.44 (C7), 133.33 (C8′a), 129.49 (C6), 127.77 (C4a), 127.53 (C2′), 127.47 (C7′), 127.28 (C5), 127.16 (C4′a), 126.18 (C1′), 125.78 (C6′), 125.48 (C8′), 124.60 (C5′), 119.65 (C_α), 119.58 (C8), 116.85 (C3), 113.89 (C3′), 56.89 (C1″), 44.98 ($N(CH_3)_2$), 31.61 (C6″), 29.89 (C2″), 29.01 (C5″), 28.96 (C4″), 26.31 (C3″), 22.51 (C7″), 14.41 (C8″).

HRMS electrospray ionization (ESI) *m*/*z* calcd for $[M + H]^+$ $C_{31}H_{37}N_2^+$ = 437.29513, found 437.29514 (mass error Δm = 0.03 ppm). The highest intensity peak is at 219.15129, which corresponds to $[M + 2H]^{2+}$ species.

3. Results and Discussion

3.1. Design and Synthesis of the Target Structure

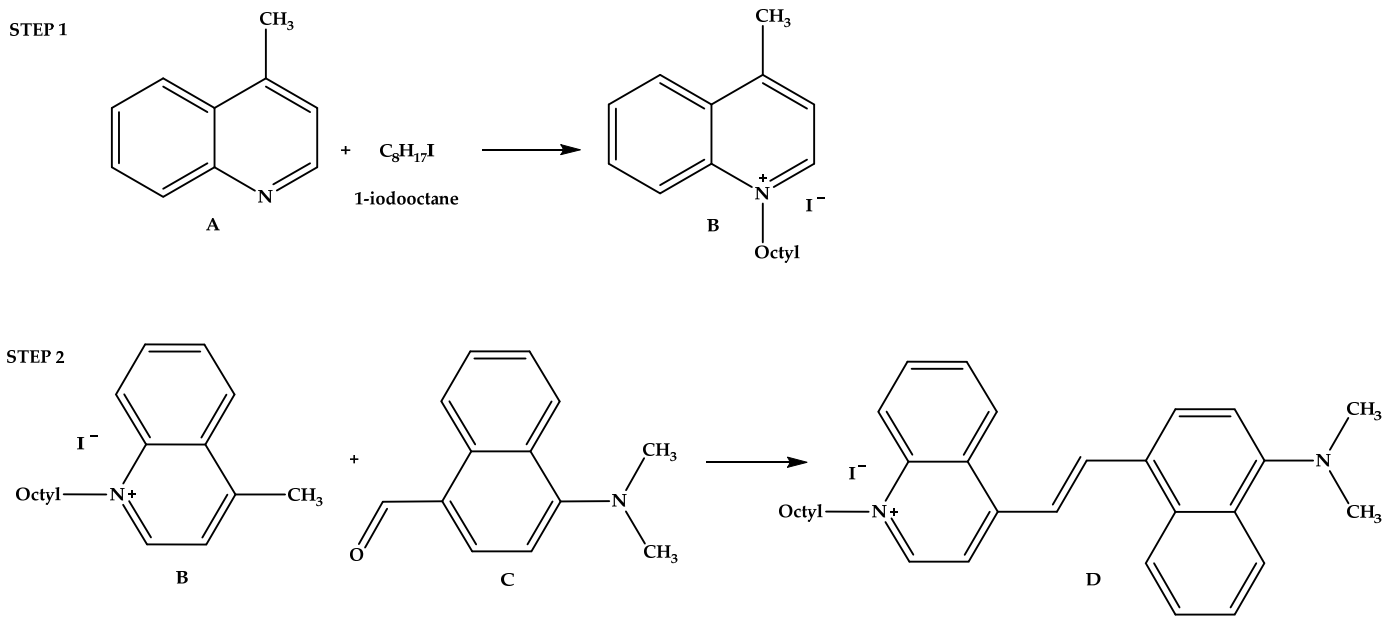
Certain structural fragments are linked to the compounds' varied actions. Based on the structural characteristics of Gram-negative bacterial cell walls and membranes, along with the chemical structure of the molecule, we have selected a dimethylamino group and a naphthalene moiety for the styrylium compound (**D**). Gram-negative bacteria

like *E. coli* and *P. aeruginosa* have hydrophobic and lipopolysaccharide-containing outer membranes. The substance can interact with membrane lipids more successfully and impair their integrity and permeability if it has a lipophilic (hydrophobic) structure. As a result, the antibacterial impact against these strains is strengthened. *P. aeruginosa* frequently exhibits resistance to numerous antibiotics, making the identification of substances with antimicrobial action very noteworthy.

The naphthalene fragment was selected due to its stable aromatic structure and lipophilic characteristics, which promote interaction with bacterial membranes and enzyme systems. Numerous naphthalene compounds also have biological activity, including antiviral, antifungal, antibacterial, and even anticancer properties [48,49]. Therefore, adding a "naphthalene moiety" to a novel compound's structure is a typical way to improve its stability and biological activity.

Considering the molecular structure of styrylquinolinium compounds and their antimicrobial properties [10,11], we investigated the synthesis of a styrylquinolinium salt with a naphthalene moiety and octyl substituent, connected to the quaternary nitrogen atom. The reason for choosing a naphthalene moiety and the octyl substituent was to increase the antimicrobial potential of the compound. Furthermore, it has been found that in some substances, the presence of an amino group improves the ability to penetrate the outer membrane of both Gram-positive and Gram-negative bacteria [11].

Compound (**D**) was synthesized through a two-step sequence (Scheme 1). First, 4-methylquinoline (lepidine, **A**) was alkylated under reflux in toluene to give N-octyl-4-methylquinolinium iodide (**B**). The iodide anion was chosen due to its large ionic radius and high polarizability, which are known to facilitate crystallization and improve crystal quality, particularly for single-crystal X-ray diffraction studies. Additionally, iodide salts of quaternary nitrogen-containing compounds are commonly used in synthetic practice due to their stability and availability. Since ion pairs are formed between the chromophore and the bulky counterion, the iodide anion can be exchanged much more readily than chlorine or bromine with bulky counterions such as toluene sulfonate, naphthalene sulfonate, etc., and is linked to potential nonlinear optical properties.



Scheme 1. Synthesis of compounds (**B**) and (**D**).

Subsequently, salt (**B**) was synthesized, followed by Knoevenagel condensation with 4-*N*,*N*-dimethylaminonaphthaldehyde (**C**) in the presence of a piperidine/acetic acid catalyst system in benzene, affording compound (**D**).

The target compound was purified by a recrystallization procedure using methanol as a solvent.

Spectroscopic techniques, including IR, 1D and 2D NMR (COSY, HSQC, and HMBC) spectra, and X-ray analysis, were used to confirm the structure of (**D**).

3.2. Spectral Analysis

3.2.1. FT-IR Spectroscopy

The IR spectrum of the target molecule (**D**) showed weak absorption bands at 3061 cm^{-1} and 3037 cm^{-1}, attributed to the C–H stretching vibrations of the two aromatic fragments—naphthalene and quinolinium—as well as the π-bridge bond (Figure S1). Intramolecular charge transfer exhibited a complicated IR spectrum around 1800 and 1400 cm^{-1}. Quantum chemistry simulations showed that most of the bands in this region are the result of mixed oscillations. The bands associated with the corresponding normal vibrations were observed to be shifted to lower wavenumbers, and some of them exhibited increased intensity. Almost all of the bands in the IR spectrum of the compound (**D**) were asymmetric due to the combined effects of the crystal field and stronger charge transfer [50].

The most intense band at 1558 cm^{-1} was assigned to the vibrations of the conjugated carbon–carbon double bond, and it is strongly mixed with the vibrations of the two aromatic rings. The degree of charge transfer between the donor and acceptor parts of the molecule affects the vibrations of the bridged double bond. Comparison of this band with the analogous band in the stilbene spectrum [51] shows a shift to the smaller wavenumber of 64 cm^{-1}, which is comparable with other binuclear compounds [51]. The band at 1596 cm^{-1} corresponds to the skeletal vibrations of the aromatic fragments. The stretching vibrations of carbon skeletons 19a and 19c appeared at 1514 cm^{-1} in the IR spectrum, which corresponds with the literature data [50,52].

3.2.2. ^{1}H and ^{13}C NMR Spectroscopy

This section outlines the two-dimensional methods used to assign the signals found in (**D**) ^{1}H- (Figure S2) and ^{13}C NMR (Figure S3) spectra. Due to the presence of two aromatic systems (quinolinic and naphthalene) and a π-bridge bond, the investigated compound (**D**) has a high number of methine protons. Consequently, we used the two-dimensional methods of ^{1}H-^{1}H correlation (COSY), ^{1}H-^{13}C correlation across one bond (HSQC), and two to three bonds (HMBC) to assign these protons with greater accuracy. The ^{1}H-NMR spectrum of compound (**D**) is shown in Figure S2 in the δ 9.4–7.2 region. Both the CH-protons from the two aromatic systems as well as the CH-vinyl protons' signals occur within this region.

The (**D**) molecule, characterized by its donor–π-bridge–acceptor structure, exhibits charge transfer from the electron-donating *N*,*N*-dimethylamino group to the positively charged nitrogen atom of the quinolinium nucleus via the π-bond system [53]. This is the reason why the protons from the two aromatic fragments of (**D**) appear in a significantly weaker field (9.36–8.65 ppm of the quinolinium part and 8.65–7.21 ppm of the naphthalene part) compared to the protons of the isolated quinolinium (δ 8.81–7.26) and naphthalene fragments (δ 7.66–7.30) [54].

Using this two-dimensional technique, we distinguished the protons from the quinoline moiety—9.36 (d), 9.09 (d), 8.80 (d), 8.54 (d), 8.25 (t), 8.03 (t)—and protons from the naphthalene part: 8.65 (d), 8.44 (d), 8.21 (d), 7.68 (t), 7.61 (t), 7.21 (d).

Analysis of the COSY spectrum (Figure S4) showed that the proton signal in the second position in the quinoline fragment was observed as a doublet at 9.36 ppm. The proton signal is observed under a lesser magnetic field due to the lower electron density at the two-site heterocyclic moiety, which is based on the positively charged nitrogen atom. The H-2 signal was correlated with proton signals at the third position H-3, and it was observed as a doublet at 8.80 ppm (Figure 2b).

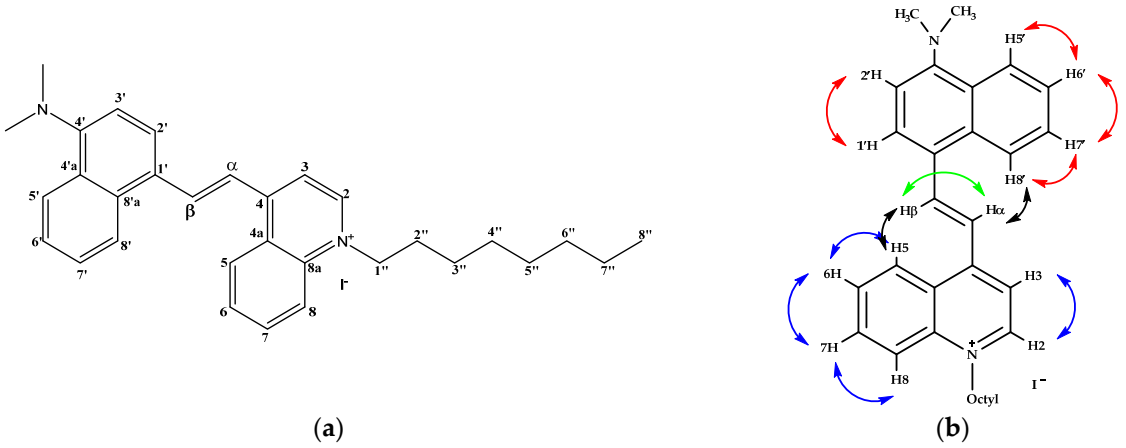


Figure 2. The numbering of atoms (**a**) and a diagram representation of the connection between the 13C and 1H atom resonances (**b**) in compound (**D**).

The signals corresponding to the H-5 proton were assigned as a doublet at 9.09 ppm. The proton H-5 showed a significant interaction with the proton H-6 detected at 8.03 ppm as a triplet. The latter has a connection to an H-7 signal at 8.25 ppm. The doublet at 8.54 ppm was attributed to the proton H-8. Proton H-2′ and H-3′ signals from the naphthalene fragment were detected as doublets at 8.45 ppm and 7.21 ppm, respectively. The triplet identified as H-6′ at 7.61 ppm was found to be interacting with the doublet defined as H-5′ at 8.21 ppm and the triplet designated as H-7′ at 7.67 ppm. The proton H-7′ interacted with the proton H-8′, the signal of which was registered as a doublet at 8.65 ppm.

Vinyl protons (H_α and H_β) from the bridging double bond register as doublets at 8.32 ppm and 8.96 ppm, exhibiting significant contact between them (Figure 2b). In addition, weak contact between protons Hβ and Hα and protons H-5 and H-8′ was observed. The *trans* configuration of the target molecule was confirmed by the high value of vinylic hydrogen J-constants. The J-constant values were found in the 13–18 Hz range, which is in good agreement with the information found in the literature [50,51].

The HSQC technique was used to determine the correlations between protons and carbons in a single bond, allowing the assignment of signals for proton-bearing carbon atoms (Figure S5). The HMBC experiment was used to attribute the signals of C-α and C-β from the bridging double bond and signals of the quaternary C-atoms at positions 4, 4a, 8a, 1′, 4a′ and 8a′, as well as the C-atom in the 4′ position to which the dimethylamino group is attached (Figure S6).

Beginning at H-2 at 9.36 ppm, the positions of the signals C-4 (153.16 ppm), C-8a (138.28 ppm), and C1″ (56.89 ppm) from the octyl tail were determined. The signal for C-8a was confirmed also via protons at C1″ (4.98 ppm), which were located at the γ-position relative to it and relative to C-2 (147.45 ppm). The proton signal H-5 at 9.09 ppm was utilized to identify the signals for C-4 (153.16) and C_α (119.65 ppm). The proton signal at the 2′ position of the naphthalene moiety was used to attribute the signals for C_β (139.95 ppm), C-8a′ (133.33 ppm) and C-4′ (154.26 ppm). The signal for the carbon atom C-8a′ was confirmed via three bonds corresponding to the proton H7′ (7.68 ppm), which is

also connected to C-5′ (124.60 ppm). Signals for hydrogen atoms H3′ (7.21 ppm) and H6′ (7.61 ppm) are positioned in the γ-position relative to C-4a′ (127.16 ppm).

Finally, the high-resolution mass spectrum of the compound showed the base peak at the m/z value, corresponding to the theoretically accurate mass of its parent ion $[M + H]^+$ in the positive mode using electrospray ionization (ESI) (Figure S7). The highest intensity peak is at 219.15129, which corresponds to $[M + 2H]^{2+}$ species.

3.2.3. Crystal Structure

Single crystals of the compound 4-[(E)-2-[4-(dimethylamino)naphthalen-1-yl]ethenyl}-1-octylquinolinium iodide, which are light red in color, were grown. The compound crystallizes in the monoclinic system; the space group is P $2_1/c$. X-ray structural data show that the unit cell contains four cations and four iodide anions. The molecular structure and atom numbering are shown in Figure 3, and Table 1 presents the crystallographic data for (**D**).

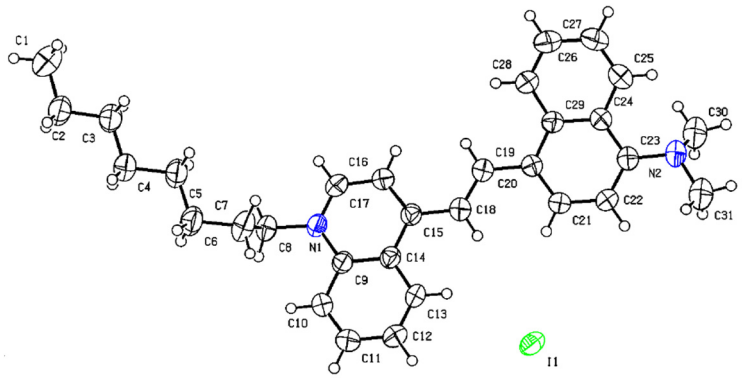


Figure 3. Molecular structure of 4-[(E)-2-[4-(dimethylamino)naphthalen-1-yl]ethenyl}-1-octylquinolinium iodide, showing the atom labeling scheme (deposition number in CCDC 2450098).

For the molecular structure of (D), the sum of the three C−N−C bond angles involving the amine nitrogen, C31-N2-C30 (110.30°), C30-N2-C23 (113.68°), and C31-N2-C23 (115.93°) is less than 360°; therefore, the dimethylamino group is not coplanar with the aromatic ring system (Table S1). Both methyl groups of the dimethylamino group show a deviation from planarity, which is also judged by the values of the measured torsion angles—C31-N2-C23-C22 is −23.45°, and C30-N2-C23-C24 is −74.56° (Table S2). Mishra et al. describe deviations of about 7° [55].

For the hemocyanine dye 1(E)-2-[4-(dimethylamino)styryl]-1-methylpyridinium triiodide [56] the sum of the three valence angles at the dimethylamino group is 360°, and the two methyl groups are coplanar, as judged by the torsion angles, which are exactly 180°. In all cases considered, the methyl groups of the dimethylamino groups participate in weak intermolecular interactions, while in compound D such interactions are absent.

The lengths of the C-N bonds in the dimethylamino group follow the trend already described for other styrene derivatives, namely that the N-CH_3 bonds are longer than the N-C (aromatic nucleus) bonds [56–60]. This confirms that the unshared electron pair of the nitrogen atom participates in delocalization with the π electrons of the naphthalene nucleus.

Table S1 shows that most valence C-C-C, C-N-C, and N-C-C angles in the conjugated aromatic system are close to trigonal, which is consistent with the crystal structure described by Zhang et al. [61].

The configuration of the double bond in the (**D**) molecule is *E (trans)*, as indicated by the value of the C16-C15-C18-C19 torsion angle of 178.47°. Most torsion angles in the molecular skeleton are close to 180°. An exception is observed in the measured torsion angles of the two aromatic nuclei relative to the bridging double bond. A deviation

from planarity is observed, as the two aromatic nuclei are twisted relative to the bridging double bond—the naphthalene at 10.33° and the quinoline at 14.82°. A possible explanation can be found in the contacts that the iodide anion makes with the molecules of the compound. One iodide anion participates in four weak intermolecular interactions with three chromophores—two contacts with the naphthalene ($C_{28}H_{28}$ ⋯ I 3.973 Å) and quinoline ($C_{16}H_{16}$ ⋯ I 3.876 Å) nuclei of one molecule; with the methylene group of the octyl tail, bound to the quaternary nitrogen atom (C_8H_8 ⋯ I 3.916 Å) of a second molecule; and with the quinoline nucleus ($C_{13}H_{13}$ ⋯ I 3.822 Å) of a third molecule.

Indicative of the delocalization in the π-electron system of the chromophore molecule are the intermediate bond lengths between the typical C−C single bond of 1.54 Å and the C=C double bond of 1.34 Å (Table S3), as well as the fact that most of the valence angles are close to 120° (Table S1).

Based on the data from the X-ray structural analysis, the structural parameter BLA of 0.13 Å (bond-length alternation) was calculated, which reflects the degree of electron delocalization, which in this case is significant and is associated with charge transfer in the **D** molecule. This, in turn, facilitates interaction with proteins, DNA, and cell membranes [62], and may affect conductivity through the cell membrane, especially in bacteria with different membrane barriers [63,64].

The parallel arrangement of the molecules two by two on the head–tail principle in the crystal lattice of (**D**), with slippage, and the quinoline nuclei arranged one above the other, is shown in Figure 4. π-π stacking interactions take place between adjacent quinolinium rings. Least-squares mean planes crossing aromatic ring atoms show an interplanar spacing of 3.533 Å. In the compound's monoclinic crystal structure, the molecules are packed in a sandwich-like pattern.

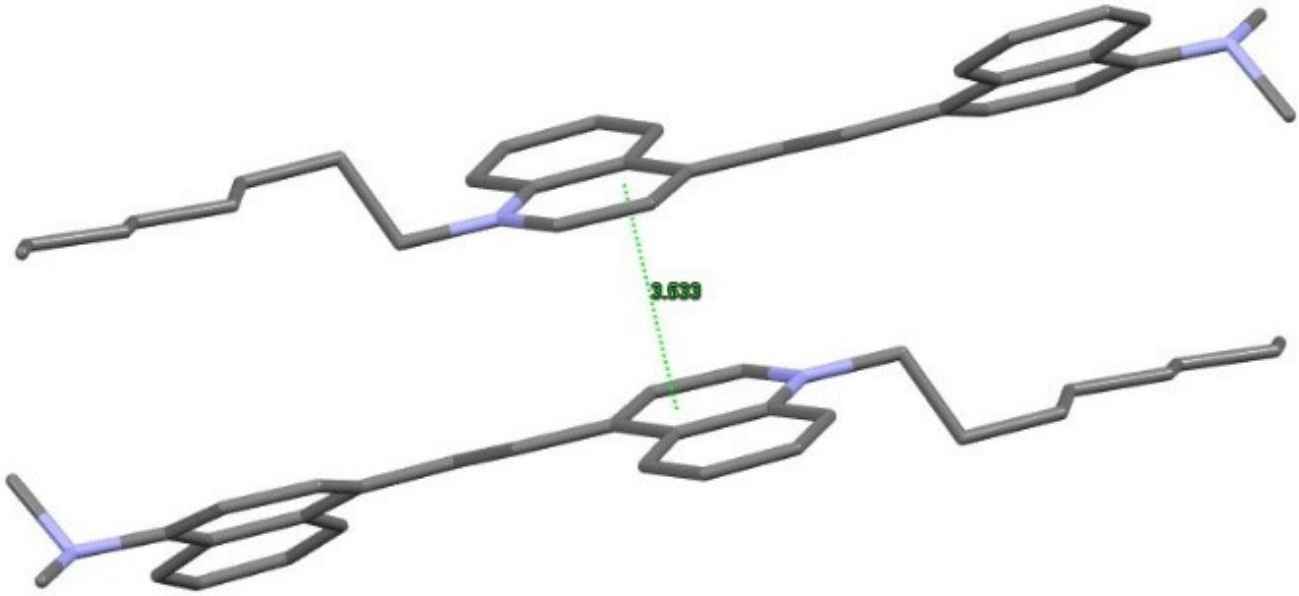


Figure 4. The parallel arrangement of the molecules.

3.2.4. DFT Perspective

To evaluate and compare the reactivity of compounds **B** and **D**, we performed structural optimizations using DFT calculations, employing the B3LYP functional in the gas phase. The absence of any imaginary harmonic frequencies in the Gaussian output confirms that both structures correspond to true energy minima. Figure 5 presents the ground-state geometries of compounds **B** and **D** as obtained from these calculations. For compound **D**, the computational and experimental values of the selected

bond lengths were estimated as follows: C30—N2 (1.439 Å/DFT and 1.440 Å/XRD), C31—N2 (1.445 Å/DFT and 1.446 Å/XRD), C23—N2 (1.418 Å/DFT and 1.418 Å/XRD), C17—N1 (1.334 Å/DFT and 1.336 Å/XRD), N1—C9 (1.381 Å/DFT and 1.382 Å/XRD), and N1—C8 (1.494 Å/DFT and 1.494 Å/XRD). For this compound, the computational and experimental values of the selected bond angles were calculated as follows: C31—N2—C30 (110.29 °/DFT and 110.30 °/XRD), C30—N2—C23 (113.69 °/DFT and 113.68 °/XRD), C31—N2—C23 (115.91 °/DFT and 115.93 °/XRD), C9—N1—C17 (120.41 °/DFT and 120.40 °/XRD), C17—N1—C8 (118.07 °/DFT and 118.04 °/XRD), and C9—N1—C8 (121.47 °/DFT and 121.52 °/XRD). These results verify that the computational and experimental structural parameters are in alignment. The optimized structures of compounds **B** and **D** exhibit total energies of −756.50 Hartree and −1313.38 Hartree, respectively, indicating their stability. Additionally, the calculated dipole moments are 2.78 Debye for compound **B** and 4.53 Debye for compound **D**. These results suggest that compound **D** exhibits a stronger dipole moment, which points to more pronounced dipole–dipole interactions in this molecule [65].

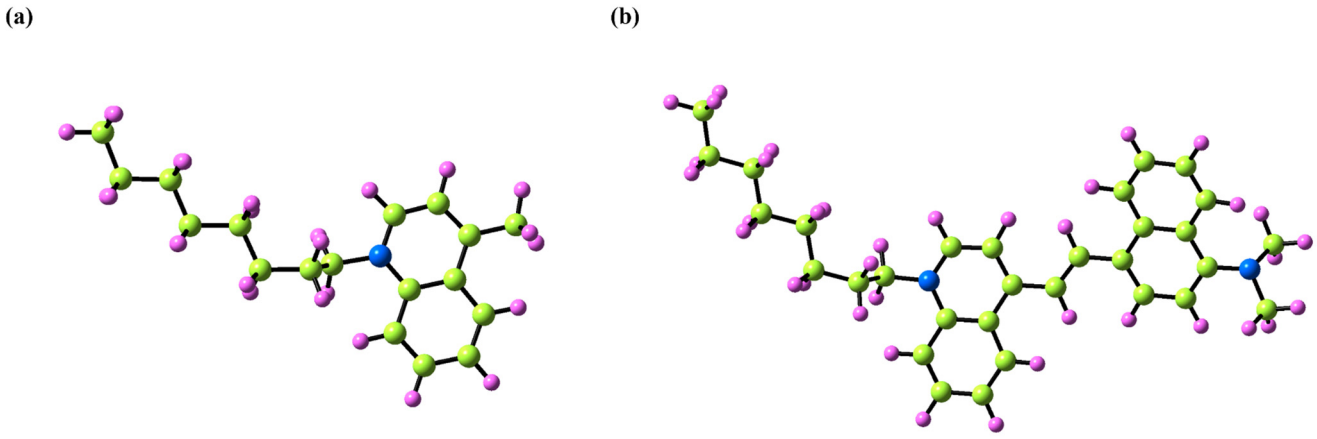


Figure 5. Suggested geometry of compounds **B** (**a**) and **D** (**b**) from DFT calculation.

The MEP surfaces of compounds **B** and **D** were predicted using the DFT/B3LYP/6-311g (d,p) computational method and are illustrated in Figure 6. These MEP maps, which offer a three-dimensional visualization of charge distribution within the molecules, provide crucial insights into regions of potential chemical reactivity and interaction [66].

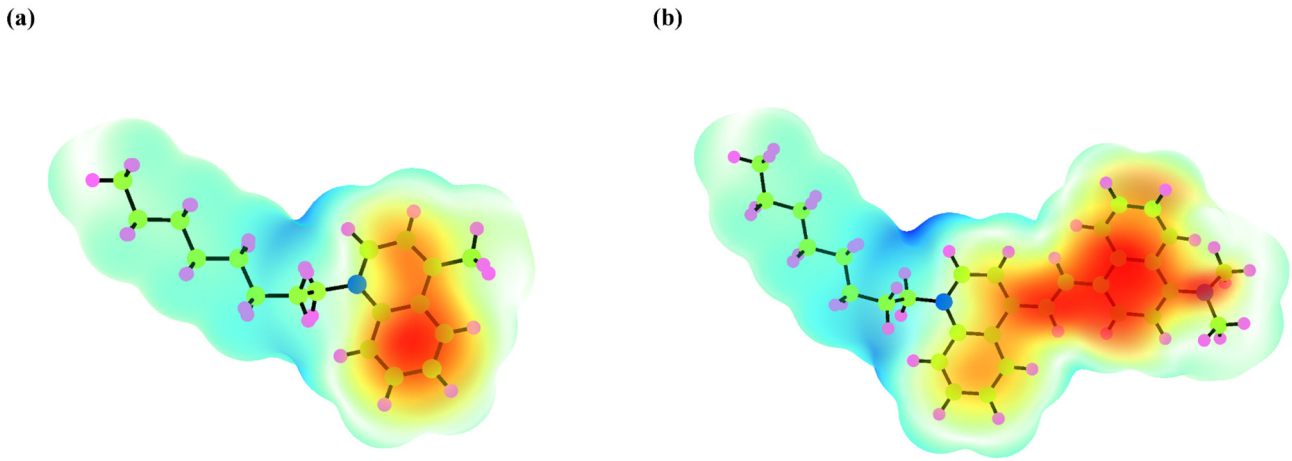


Figure 6. MEPs of compounds **B** (**a**) and **D** (**b**).

MEP analysis is particularly useful for identifying sites likely to engage in hydrogen bonding, as well as for locating areas susceptible to nucleophilic or electrophilic attacks. The surfaces display a spectrum of electrostatic potentials through color gradients ranging from blue to red. The blue regions indicate electron-deficient zones with a positive electrostatic potential, while red regions represent electron-rich areas with negative potential [67]. Neutral regions, with no significant charge density, appear green [68]. In this context, red areas tend to attract electrophiles, whereas blue regions are favorable for nucleophiles, as these colors denote the respective reactive behavior of nucleophilic and electrophilic sites. In the MEP maps of compounds **B** and **D**, the red coloration is predominantly distributed around the naphthalene moiety, suggesting that this region is favorable for electrophilic attack.

Figure 7 illustrates the distribution patterns and energy profiles of the HOMO and LUMO orbitals for compounds **B** and **D**, based on calculations performed using the TD-DFT/B3LYP/6-311g (d,p) method. These frontier orbitals, HOMO and LUMO, play a pivotal role in defining a molecule's electronic behavior, influencing its biological activity, chemical reactivity, and overall stability [69]. The HOMO serves as an electron donor, while the LUMO acts as an electron acceptor. The energy difference between them, represented by E_{gap}, provides valuable insight into the molecule's potential reactivity and activity. A smaller E_{gap} indicates a greater ease of electron transition, which typically correlates with increased chemical and biological activity, but reduced molecular stability. In both compounds **B** and **D**, the distribution of the HOMO and LUMO electron clouds is primarily localized on the naphthalene unit, suggesting that electron transfer is concentrated in this region. The measured energy gaps for compounds **B** and **D** are 4.87 and 3.28 eV, respectively. The small energy difference between the HOMO and LUMO levels of push–pull compounds of the **D** type has been confirmed by experimental studies based on data from UV–visible spectrum and electrochemical tests [20]. The smaller band gap in compound D indicates greater chemical reactivity and enhanced biological activity compared to compound **B**. Additionally, the lower ΔE value in compound **D** facilitates more efficient charge transfer, which further supports its higher level of biological activity [70].

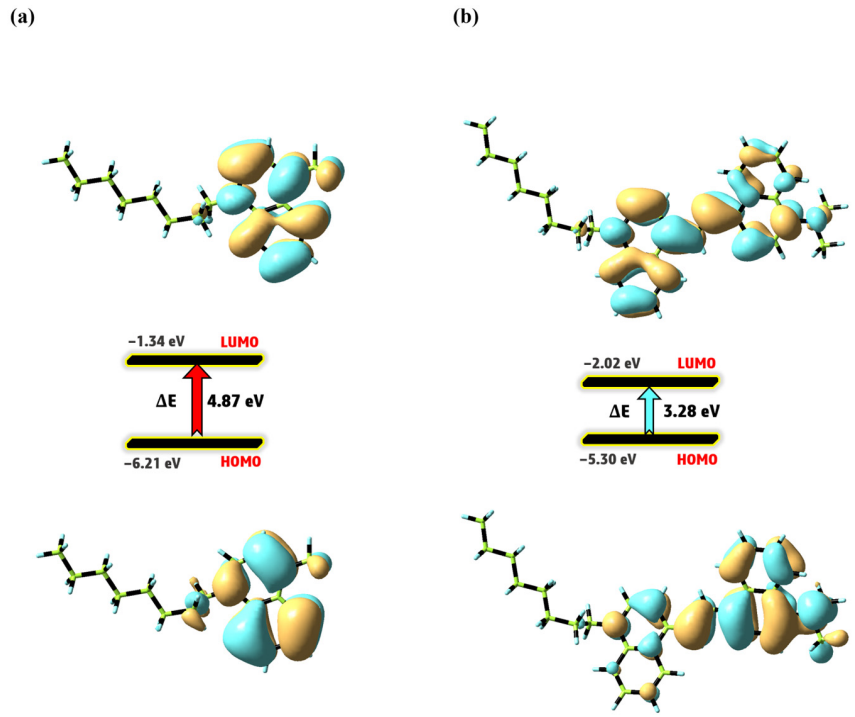


Figure 7. Distributions and energy surfaces of the molecular orbitals of compounds **B** (**a**) and **D** (**b**).

Figure 8 shows a schematic illustration of the excited state (quinoid form) and ground state (benzoid form) of the chromophore of compound **D** as a result of charge transfer from the electron-donating N, N-dimethylamino group through the π-conjugated system to the electron-accepting quinoline nucleus [52].

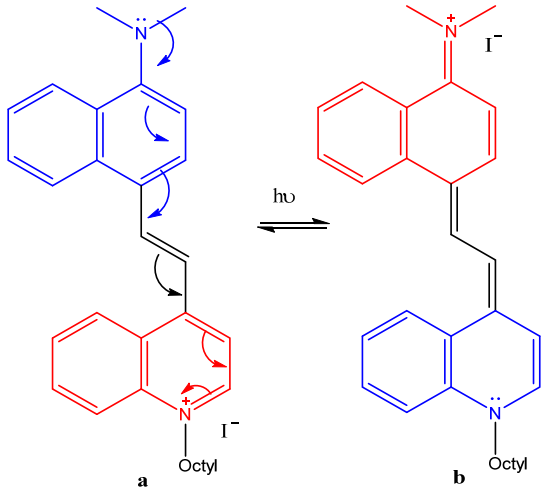
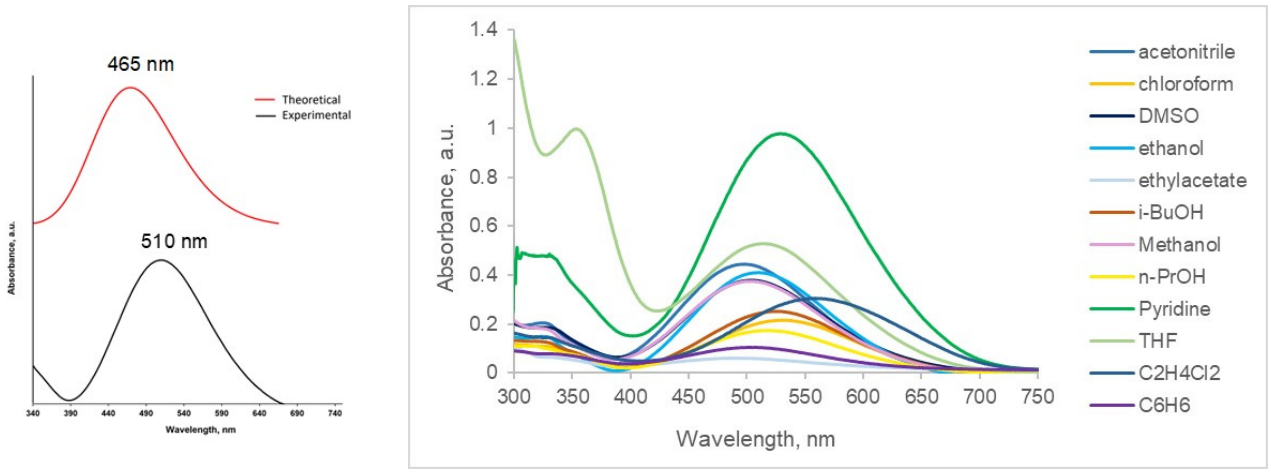


Figure 8. Ground state (benzoid form) (**a**) and excited state (quinoid form) (**b**) of the chromophore of compound (**D**).

In the UV–visible spectrum of compound (**D**) (Figure 9), the absorption maximum at around 500 nm corresponds to the charge transfer band, with the observed shift depending on the polarity of the solvent, which is explained by the fact that the polarity, polarizability, and hydrogen-bonding ability of the solvents can change the HOMO–LUMO energy difference and, accordingly, shift the energy of the equilibrium excited state [50,51].



(**a**) (**b**)

Figure 9. Theoretical (**a**) and experimental (**b**) UV-Vis spectra of compound (**D**) in ethanol.

Using DFT insight, several quantum chemical reactivity descriptors were determined, including absolute electronegativity (χ), softness (σ), the global electrophilicity index (ω), chemical potential (P_i), hardness (η), and the maximum charge transfer (ΔN_{max}), in accordance with equations outlined in previous studies (Table 2) [71]. The negative P_i values indicate that the analyzed compounds possess stability. The global electrophilicity index (ω) reflects a molecule's tendency to accept electrons from its environment. A higher ω value suggests a stronger capability to form various interactions with biological macromolecules. Compound (**D**) exhibits a higher electrophilicity (4.08 eV) than compound B (2.92 eV),

indicating a greater potential to engage with targets like proteins. The parameter ΔN_{max} estimates the maximum number of electrons one compound can accept. Compound (**D**) displays a ΔN_{max} of 2.23, compared to 1.55 for compound **B**, suggesting superior electron-accepting behavior. These results collectively indicate that compound (**D**) demonstrates a more favorable electronic interaction profile than compound **B**.

Table 2. Quantum reactivity parameters of compounds **B** and **D**.

Parameter	Compound B	Compound D
E_{HOMO}	−6.21	−5.30
E_{LUMO}	−1.34	−2.02
$E_{gap\ (LUMO-HOMO)}$	4.87	3.28
χ	3.77	3.66
η	2.43	1.64
σ	0.41	0.61
P_i	−3.77	−3.66
ω	2.92	4.08
ΔN_{max}	1.55	2.23

The UV-Vis spectrum of the compound was calculated using time-dependent density functional theory (TD-DFT) with the CPCM solvation model, employing ethanol as the solvent. The resulting spectrum is shown in Figure 9a and exhibits good agreement with the experimental UV-Vis spectrum of the compound (**D**) (Figure 9b).

3.3. Antimicrobial Activity

The agar diffusion technique was used to examine the antibacterial activity of the novel styrylquinolinium on five Gram-positive bacterial strains, five Gram-negative bacterial strains, two yeasts, and six fungi. The well diffusion method reveals the level of sensitivity in pathogenic microorganisms. Therefore, an organism susceptible to a chemical will not develop near the well where it was placed. The mean zones of inhibition in mm produced on the pathogenic microorganisms containing styrylquinolinium are presented in Table 3.

Our results illustrate that styrylquinolinium exhibited good antimicrobial activity against the Gram-positive bacterial strains *Bacillus subtilis* (inhibition zone = 13 mm), *Bacillus amyloliquefaciens* (inhibition zone = 13 mm), *Staphylococcus aureus* (inhibition zone = 14 mm), *Listeria monocytogenes* (inhibition zone = 13 mm), and *Enterococcus faecalis* (inhibition zone = 13 mm) and the Gram-negative strains *Salmonella enteritidis* (inhibition zone = 13 mm), and *Escherichia coli* (inhibition zone = 16 mm). Additionally, it demonstrated very good activity against pathogenic *Pseudomonas aeruginosa* (inhibition zone = 20 mm) (Table 3). This difference in activity can be attributed to the difference in cell membrane permeability between the Gram-positive and Gram-negative bacterial strains, which is significantly affected by complex factors, including the zeta potential on the membrane, the lipophobicity of the cell membrane, the thickness of the membrane and its surrounding layers, and the chemical composition of the antimicrobial drug [72].

The outcomes of the minimum inhibitory concentration for (**D**) are shown in Table 4. (**D**)'s MIC was 7.8 µg/mL for the Gram-positive bacteria *Bacillus subtilis*, *Bacillus amyloliquefaciens*, *Staphylococcus aureus*, and *Listeria monocytogenes* and fully consistent with the literature data for styrylquinolinium compounds (2.4 to 75 µg/mL). Styrylquinolinium compounds most often do not exhibit antibacterial activity against Gram-negative bacteria, including *Pseudomonas aeruginosa*, which is prone to developing antibiotic resistance. In our experiments, the target compound (**D**) inhibits *Pseudomonas aeruginosa* (MIC 7.8 µg/mL). (**D**) showed antimicrobial activity against *Salmonella enteritidis* (MIC 31 µg/mL), with no literature data available on this. Additionally, it exhibits three times the activity of compa-

rable drugs against *Escherichia coli* (MIC 7.8 μg/mL) [10,11]. The likely explanation for this difference relates to the different structural fragments in (**D**) and other styrylquinolinium compounds. Compound (**D**) has a naphthalene core and an octyl substituent, while most of the other styryliums have a pyridinium core and shorter carbon chain substituents.

Table 3. Antimicrobial activity of the synthesized styrylquinolinium D.

Bacteria	Inhibition Zones, mm			
	24 h	48 h	N	A
Bacillus subtilis	13	13	n.a.	16
Bacillus amyloliquefaciens	13	13	n.a.	20
Staphylococcus aureus	14	13	n.a.	35
Listeria monocytogenes	13	13	n.a.	40
Enterococcus faecalis	13	13	n.a.	38
Salmonella enteritidis	13	13	n.a.	40
Klebsiella spp.	ND	ND	n.a.	25
Escherichia coli	16	16	n.a.	16
Proteus vulgaris	ND	ND	n.a.	30
Pseudomonas aeruginosa	20	20	n.a.	16
Candida albicans	12	12	22	n.a.
Saccharomyces cerevisiae	8	8	31	n.a.
Aspergillus niger	15	15	32	n.a.
Aspergillus flavus	13	13	26	n.a.
Penicillium spp.	8	8	26	n.a.
Rhizopus spp.	12	12	n.a.	n.a.
Fusarium moniliforme	12	12	25	n.a.

ND—no activity detected; N—Nystatin; A—Ampicillin; n.a.—not applicable.

Table 4. MIC of D against Gram-positive and Gram-negative bacterial strains.

Bacteria	MIC, μg/mL
Bacillus subtilis	7.8
Bacillus amyloliquefaciens	7.8
Staphylococcus aureus	7.8
Listeria monocytogenes	7.8
Enterococcus faecalis	31
Salmonella enteritidis	31
Klebsiella spp.	ND
Escherichia coli	7.8
Proteus vulgaris	ND
Pseudomonas aeruginosa	7.8
Candida albicans	15
Saccharomyces cerevisiae	ND
Aspergillus niger	15
Aspergillus flavus	15
Penicillium spp.	250
Rhizopus spp.	31
Fusarium moniliforme	15
Mucor spp.	ND

Our results showed that (**D**) does not exhibit activity against *Klebsiella pneumoniae* and *Proteus vulgaris*, which is confirmed by the literature data for previously synthesized styrylium compounds [10,11].

Studies on the antifungal activity of styrylpyridinium salts are limited [73], and there are no studies on styrylquinolinium salts. Substituted styrylpyridinium salts have been demonstrated to exhibit activity against *Candida albicans*. Our experiments have

demonstrated that the styrylquinolinium (**D**) exhibited moderate activity against *Candida albicans* (MIC 15 µg/mL). (**D**) also exhibited moderate activity against *Aspergillus niger* (MIC 15 µg/mL), *Aspergillus flavus* (MIC 15 µg/mL), *Fusarium moniliforme* (MIC 15 µg/mL), and *Rhizopus spp.* (MIC 31 µg/mL).

3.4. Molecular Docking Modeling

Given that in vitro studies demonstrated that the synthesized compound (**D**) exhibits notable antibacterial activity against *E. coli*, we utilized molecular docking simulations to validate these findings and to identify key interactions within the binding environment. To evaluate the antibacterial potential of compound (**D**), molecular docking studies were conducted targeting the *Escherichia coli* protein (PDB ID: 2VF5). Among the various binding conformations generated, those exhibiting the most favorable (i.e., most negative) binding free energies were selected for detailed interaction analysis. The optimal binding conformation of compound (**D**) with the *E. coli* protein was examined to identify the key molecular interactions involved, as depicted in Figure 10. The simulation results revealed that compound (**D**) binds effectively to the active site of the bacterial protein, with a calculated binding free energy of −6.60 kcal/mol. This value reflects a good binding affinity, supporting the experimental findings of the compound's antibacterial activity. Furthermore, compound (**D**) forms seven hydrophobic interactions involving residues LEU 484, LYS 487, LEU 601, HIS 493, and HIS 466, as well as seven van der Waals contacts with amino acids GLY 301, CYS 300, THR 302, GLU 488, PRO 598, ARG 599, and TYR 491.

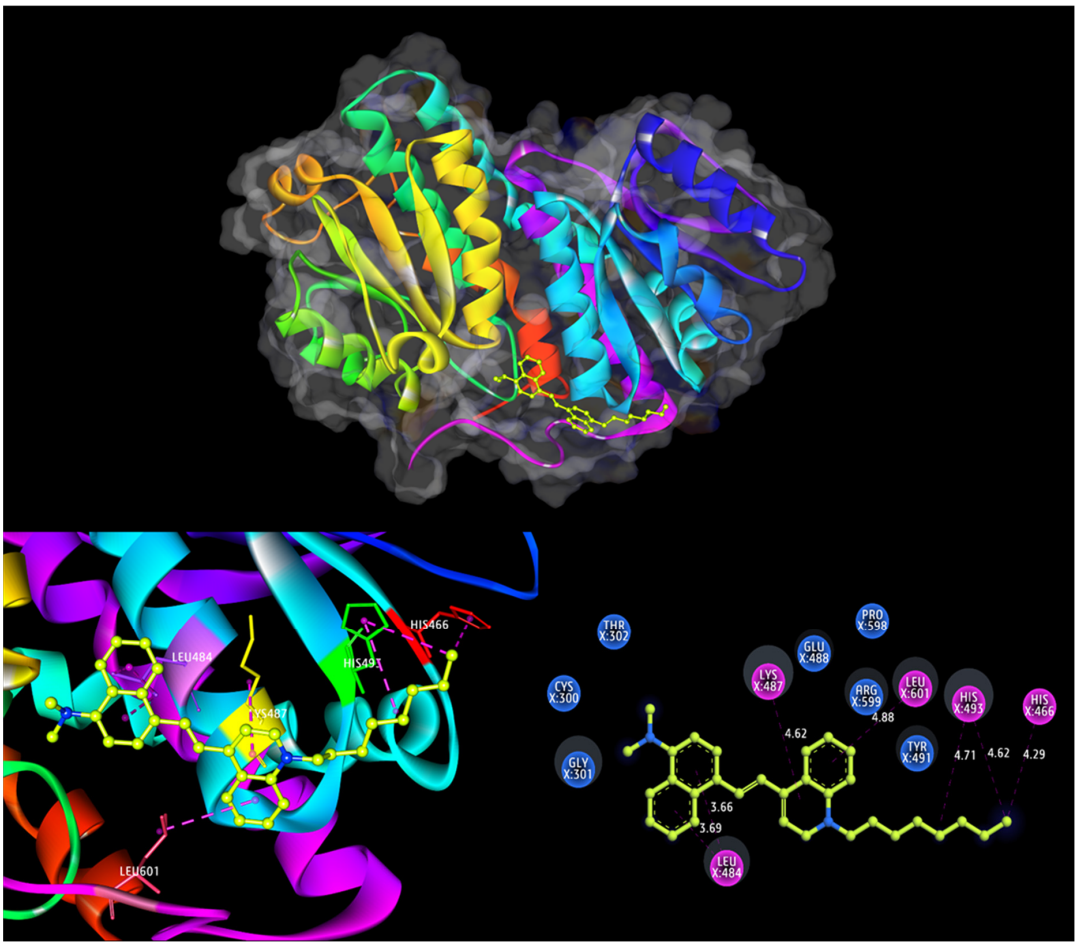


Figure 10. Docking analysis of compound (**D**) in the interaction with *E. coli*.

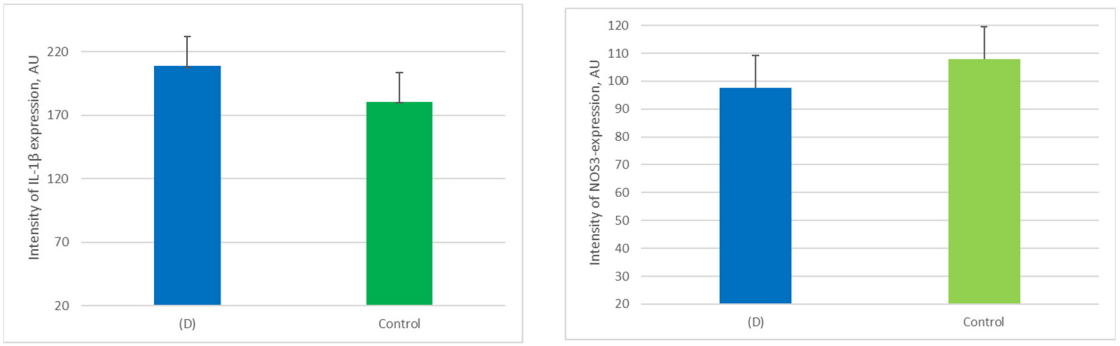
3.5. Anti-Inflammatory Activity

Inflammation is the body's defensive reaction to irritants, infections, or tissue damage. Cytokines are among the many mediators that are crucial to this process. For example, IL-1β is a proinflammatory cytokine known for triggering an immune response and sustaining the innate response. When an infection or injury occurs, activated macrophages and monocytes are the primary sources of the powerful inflammatory cytokine IL-1β. It contributes significantly to the development of inflammation and is linked to a number of chronic illnesses, including atherosclerosis, Crohn's disease, and rheumatoid arthritis [74].

Proinflammatory cytokines IL-1α and IL-1β are generated either in response to innate identification of Pathogen-Associated Molecular Patterns (PAMPs) or after host injury (release of Damage-Associated Molecular Patterns (DAMPs)). The adaptive immune response is shaped by IL-1 activity on T cells and Dendritic cells (DCs). Although DCs' capacity to trigger T-cell activation is enhanced by IL-1 signaling, direct IL-1 activity on CD4+ and CD8+ T cells, either by itself or in combination with other polarizing cytokines, has also been shown to affect T-cell differentiation in a number of circumstances. Since IL-1 functions as a direct link between innate and adaptive immunity, it can be used clinically to support T-cell immunity development in the context of preventative and therapeutic measures [75–77].

Since IL-1β plays a key role in both autoimmune and inflammatory illnesses, inhibiting its activity is crucial for lowering the inflammatory response [78].

The immunohistological expression of IL-1β and NOS3 in smooth muscle (SM) preparations treated with the novel styrylquinolinium compound (**D**) was evaluated using a quantitative test (Figure 11). In preparations treated with (**D**), SM cells and the MP showed higher expression of IL-1β (208.71 ± 21 AU) compared to controls (180.54 ± 23 AU) (Figure 11a).



(**a**) (**b**)

Figure 11. Morphometric analysis of (**a**) IL-1β and (**b**) NOS3 immunoreactivity in gastric tissues after treatment with substance (D). Values are presented in arbitrary units (AU) as mean ± SD (n = 3).

Preparations incubated with (**D**) decreased expression of NOS3 (98.13 ± 11.7 AU) in SM cells and the myenteric plexus (MP) (Figure 11b) compared to control preparations (108.3 ± 19.01 AU).

Immunohistochemical analysis showed that treatment with styrylquinolinium (**D**) resulted in increased expression of IL-1β and a modest decrease in NOS3 in smooth muscle cells and the MP. These changes suggest that the compound possesses immunomodulatory activity, concomitant with its antimicrobial effect. IL-1β is a key proinflammatory cytokine involved in the initiation of the innate immune response, activation of macrophages, and homing of neutrophils to the site of inflammation [79]. Its increase during incubation with substance D may help the body fight off infections locally. Its direct antibacterial effect against bacteria like *P. aeruginosa* and *E. coli* can be explained by this fact. According to

Dinarello, IL-1β is a "central axis" in inflammatory processes and is often a desirable target for immunotherapies [80].

NOS3 (endothelial NO synthase) is responsible for the production of nitric oxide (NO), which has anti-inflammatory and vasodilating effects [80]. The decreased expression of NOS3 upon (**D**) treatment was not drastic, suggesting a temporary upregulation rather than a suppression of function. This may reflect an adaptive mechanism to limit excessive vasodilation in the immune response.

According to the immunomodulatory tests, compound (**D**) may have an impact on inflammatory mediators, as evidenced by variations in the expression of NOS3 and IL-1β. However, these findings should be considered suggestive and require more research before firm conclusions about the compound's immunomodulatory potential can be made because of the observed variability in the data.

4. Conclusions

A novel styrylquinolinium salt 4-[(E)-2-(4-dimethylaminonaphthalen-1-yl)ethenyl)]-1-octyl-quinolinium iodide (**D**) was synthesized. The target compound (**D**) was obtained by sequential application of the alkylation and Knoevenagel reactions. IR, mono- and two-dimensional NMR, and HRMS techniques were utilized to clarify its molecular structure. The X-ray analysis confirmed the structure of the compound.

According to the preliminary biological analysis and MIC data, compound (**D**) has antibacterial activity against selected Gram-negative bacteria, such as *Salmonella enteritidis*, *Escherichia coli*, and *Pseudomonas aeruginosa*. Furthermore, significant antifungal activity was found against a number of fungal species, including *Fusarium moniliforme*, *Aspergillus niger*, *Aspergillus flavus*, *Rhizopus* spp., and *Candida albicans*.

Furthermore, docking simulation revealed that compound (**D**) binds effectively to the active site of the bacterial protein, with a calculated binding free energy of −6.60 kcal/mol, supporting the experimental findings of the compound's antibacterial activity. Based on molecular docking, the activity of the compound against *Escherichia coli* is explained by the ability to bind through hydrophobic interactions with amino acid residues of the bacterial protein and thus to destroy the cell wall.

Based on the immunomodulatory assays, we can conclude that (**D**) may affect inflammatory mediators, as evidenced by variations in the expression of IL-1β and NOS3. However, further investigation is required before definitive conclusions can be drawn regarding the immunomodulatory potential of the compound.

Supplementary Materials: The following supporting information can be downloaded at https://www.mdpi.com/article/10.3390/cryst16020115/s1, Figure S1. IR spectrum of D; Figure S2. ^{1}H- spectrum of (**D**); Figure S3. ^{13}C- spectrum of (**D**); Figure S4. COSY spectrum of D; Figure S5. HSQC spectrum of (**D**); Figure S6. HMBC spectrum of (**D**); Figure S7. HR-ESI-MS spectrum; Table S1. Selected angles (°) for (**D**); Table S2. Selected torsion angles (°) for (**D**); Table S3. Selected bond lengths (Å) for (**D**).

Author Contributions: Conceptualization, M.T., R.B. and T.K.; methodology, S.Z., M.T. and R.B.; formal analysis, M.P., S.Z., Y.T., P.N., F.A. and E.C.; investigation, S.N., S.Z., M.P., Y.T., P.N., F.A. and E.C.; software, M.F.-D. and S.S.; visualization, M.F.-D. and M.P.; resources—P.N., F.A., M.F.-D.; writing—original draft preparation, M.T., E.C., S.N., M.P. and M.F.-D.; writing—review and editing, S.N.; supervision, M.T. and S.N.; project administration—M.T. and S.N. All authors have read and agreed to the published version of the manuscript.

Funding: This research received no external funding.

Institutional Review Board Statement: The Local Ethics Committee approved the study protocol (Ethical Committee of the Bulgarian Food Agency with No400/23 May 2024). All studies were

conducted according to the Institutional Animal Care guidelines and complied with the EU Directive 2010/63/EU. All experiments were carried out according to the legislation on the Welfare and Protection of Animals Used for Experimental and Other Scientific Purposes. All efforts were made to minimize the number of animals used.

Data Availability Statement: The original contributions presented in this study are included in the article/Supplementary Material. Further inquiries can be directed to the corresponding authors.

Acknowledgments: This study is part of Scientific Project No KP-06-H73/11 of the National Fund for Scientific Research in Bulgaria, National Program for Basic Research Projects—2023.

Conflicts of Interest: The authors declare no conflicts of interest.

References

1. World Health Organization. *World Health Statistics 2015*; World Health Organization (WHO Press): Geneva, Switzerland, 2015; Chapter 1; pp. 11–25, ISBN 978-92-4-156488-5.
2. Andersson, J.A.; Fitts, E.C.; Kirtley, M.L.; Ponnusamy, D.; Peniche, A.G.; Dann, S.M.; Motin, V.L.; Chauhan, S.; Rosenzweig, J.A.; Sha, J.; et al. New Role for FDA-Approved Drugs in Combating Antibiotic-Resistant Bacteria. *Antimicrob. Agents Chemother.* **2016**, *60*, 3717–3729. [CrossRef]
3. Tanwar, J.; Das, S.; Fatima, Z.; Hameed, S. Multidrug resistance: An emerging crisis. *Interdiscip. Perspect. Infect. Dis.* **2014**, *2014*, 541340. [CrossRef]
4. Thi, M.T.T.; Wibowo, D.; Rehm, B.H.A. *Pseudomonas aeruginosa* Biofilms. *Int. J. Mol. Sci.* **2020**, *21*, 8671. [CrossRef] [PubMed]
5. De Oliveira, D.M.P.; Forde, B.M.; Kidd, T.J.; Harris, P.N.A.; Schembri, M.A.; Beatson, S.A.; Paterson, D.L.; Walker, M.J. Antimicrobial Resistance in ESKAPE Pathogens. *Clin. Microbiol. Rev.* **2020**, *33*. [CrossRef] [PubMed]
6. Zakhour, J.; Sharara, S.L.; Hindy, J.R.; Haddad, S.F.; Kanj, S.S. Antimicrobial Treatment of *Pseudomonas aeruginosa* Severe Sepsis. *Antibiotics* **2022**, *11*, 1432. [CrossRef]
7. Silby, M.W.; Winstanley, C.; Godfrey, S.A.; Levy, S.B.; Jackson, R.W. *Pseudomonas* Genomes: Diverse and Adaptable. *FEMS Microbiol. Rev.* **2011**, *35*, 652–680. [CrossRef]
8. Rossi, E.; La Rosa, R.; Bartell, J.A.; Marvig, R.L.; Haagensen, J.A.J.; Sommer, L.M.; Molin, S.; Johansen, H.K. *Pseudomonas aeruginosa* Adaptation and Evolution in Patients with Cystic Fibrosis. *Nat. Rev. Microbiol.* **2021**, *19*, 331–342. [CrossRef]
9. Jurado-Martin, I.; Sainz-Mejias, M.; McClean, S. *Pseudomonas aeruginosa*: An Audacious Pathogen with an Adaptable Arsenal of Virulence Factors. *Int. J. Mol. Sci.* **2021**, *22*, 3128. [CrossRef] [PubMed]
10. Cendra, M.D.M.; Torrents, E. *Pseudomonas aeruginosa* Biofilms and Their Partners in Crime. *Biotechnol. Adv.* **2021**, *49*, 107734. [CrossRef] [PubMed]
11. Moradali, M.F.; Ghods, S.; Rehm, B.H.A. *Pseudomonas aeruginosa* Lifestyle: A Paradigm for Adaptation, Survival, and Persistence. *Front. Cell. Infect. Microbiol.* **2017**, *7*, 39. [CrossRef]
12. Reynolds, D.; Kollef, M. The Epidemiology, Pathogenesis and Treatment of *Pseudomonas aeruginosa* Infections: An Update. *Drugs* **2021**, *81*, 2117–2131. [CrossRef]
13. Pang, Z.; Raudonis, R.; Glick, B.R.; Lin, T.J.; Cheng, Z. Antibiotic Resistance in *Pseudomonas aeruginosa*: Mechanisms and Alternative Therapeutic Strategies. *Biotechnol. Adv.* **2019**, *37*, 177–192. [CrossRef]
14. Blomquist, K.C.; Nix, D.E. A Critical Evaluation of Newer Beta-Lactam Antibiotics for Treatment of *Pseudomonas aeruginosa* Infections. *Ann. Pharmacother.* **2021**, *55*, 1010–1024. [CrossRef]
15. Wilson, M.G.; Pandey, S. *Pseudomonas aeruginosa*. In *StatPearls [Internet]*; StatPearls Publishing: Treasure Island, FL, USA, 2025. Available online: https://www.ncbi.nlm.nih.gov/books/NBK557831/ (accessed on 25 January 2025).
16. Avakh, A.; Grant, G.D.; Cheesman, M.J.; Kalkundri, T.; Hall, S. The Art of War with *Pseudomonas aeruginosa*: Targeting Mex Efflux Pumps Directly to Strategically Enhance Antipseudomonal Drug Efficacy. *Antibiotics* **2023**, *12*, 1304. [CrossRef]
17. Murray, C.J.L.; Ikuta, K.S.; Sharara, F.; Swetschinski, L.; Aguilar, G.R.; Gray, A.; Han, C.; Bisignano, C.; Rao, P.; Wool, E.; et al. Global Burden of Bacterial Antimicrobial Resistance in 2019: A Systematic Analysis. *Lancet* **2022**, *399*, 629–655. [CrossRef] [PubMed]
18. Tacconelli, E.; Carrara, E.; Savoldi, A.; Harbarth, S.; Mendelson, M.; Monnet, D.L.; Pulcini, C.; Kahlmeter, G.; Kluytmans, J.; Carmeli, Y.; et al. Discovery, Research, and Development of New Antibiotics: The WHO Priority List of Antibiotic-Resistant Bacteria and Tuberculosis. *Lancet Infect. Dis.* **2018**, *18*, 318–327. [CrossRef] [PubMed]
19. Daikos, G.L.; da Cunha, C.A.; Rossolini, G.M.; Stone, G.G.; Baillon-Plot, N.; Tawadrous, M.; Irani, P. Review of Ceftazidime-Avibactam for the Treatment of Infections Caused by *Pseudomonas aeruginosa*. *Antibiotics* **2021**, *10*, 1126. [CrossRef]
20. Wessels, S.; Ingmer, H. Modes of action of three disinfectant active substances: A review. *Regul. Toxicol. Pharmacol.* **2013**, *67*, 456–467. [CrossRef] [PubMed]

21. Jiao, Y.; Niu, L.N.; Ma, S.; Li, J.; Tay, F.R.; Chen, J.H. Quaternary ammonium-based biomedical materials: State-of-the-art, toxicological aspects and antimicrobial resistance. *Prog. Polym. Sci.* **2017**, *71*, 53–90. [CrossRef]
22. Kula, N.; Lamch, L.; Futoma-Kołoch, B.; Wilk, K.A.; Obłąk, E. The effectiveness of newly synthesized quaternary ammonium salts differing in chain length and type of counterion against priority human pathogens. *Sci. Rep.* **2022**, *12*, 21799. [CrossRef]
23. Choquet-Kastylevsky, G.; Vial, T.; Descotes, J. Allergic adverse reactions to sulfonamides. *Curr. Allergy Asthma Rep.* **2002**, *2*, 15–25. [CrossRef]
24. Wyrzykiewicz, E.; Wendzonka, M.; Kedzia, B. Synthesis and antimicrobial activity of new (E)-4-[piperidino (4′-methylpiperidino-, morpholino-) N-alkoxy]stilbenes. *Eur. J. Med. Chem.* **2006**, *41*, 519–525. [CrossRef] [PubMed]
25. Chanawanno, K.; Chantrapromma, S.; Anantapong, T.; Kanjana-Opas, A.; Fun, H. Synthesis, Structure and In Vitro Antibacterial Activities of New Hybrid Disinfectants Quaternary Ammonium Compounds: Pyridinium and Quinolinium Stilbene Benzenesulfonates. *Eur. J. Med. Chem.* **2010**, *45*, 4199–4208. [CrossRef]
26. Kim, E.; Lee, S.; Lee, S.; Kwon, O.-P.; Yoon, H. New Antibacterial-Core Structures Based on Styryl Quinolinium. *Food Sci. Biotechnol.* **2017**, *26*, 521–529. [CrossRef]
27. Li, Y.; Li, Z.-R.; Wu, D.; Li, R.-Y.; Hao, X.-Y.; Sun, C.-C. An ab Initio Prediction of the Extraordinary Static First Hyperpo-larizability for the Electron-Solvated Cluster $(FH)_2^-${e}(HF). *J. Phys. Chem. B* **2004**, *108*, 3145–3150. [CrossRef]
28. Supabowornsathit, K.; Faikhruea, K.; Ditmangklo, B. Dicationic Styryl Dyes for Colorimetric and Fluorescent Detection of Nucleic Acids. *Sci. Rep.* **2022**, *12*, 14250. [CrossRef] [PubMed]
29. Kim, Y.-H.; Youk, J.-S.; Kim, S.-H.; Chang, S.-K. Solvatochromic Fluorescence Behavior of 8-Aminoquinoline-Benzothiazole: A Sensitive Probe for Water Composition in Binary Aqueous Solutions. *Bull. Korean Chem. Soc.* **2005**, *26*, 47–50. [CrossRef]
30. Collot, M.; Boutant, E.; Fam, K.T.; Danglot, L.; Klymchenko, A.S. Molecular Tuning of Styryl Dyes Leads to Versatile and Efficient Plasma Membrane Probes for Cell and Tissue Imaging. *Bioconjugate Chem.* **2020**, *31*, 875–883. [CrossRef]
31. Nuntavanotayan, N.; Nakprasit, K.; Israsena, N.; Rungrotmongkol, T.; Chuawong, P.; Vilaivan, T.; Aonbangkhen, C. Design, Synthesis, and Characterization of Novel Styryl Dyes as Fluorescent Probes for Tau Aggregate Detection in Vitro and in Cells. *Chem. Asian J.* **2024**, *19*, e202301081. [CrossRef]
32. Efimova, A.S.; Ustimova, M.A.; Chmelyuk, N.S.; Abakumov, M.A.; Fedorov, Y.V.; Fedorova, O.A. Specific Fluorescent Probes for Imaging DNA in Cell-Free Solution and in Mitochondria in Living Cells. *Biosensors* **2023**, *13*, 734. [CrossRef]
33. Zhang, C.; Yu, Z.; Liu, Y.; Jin, W.; Liu, Z.; Yu, X. Rigidify Styryl-Pyridinium Dyes to Benzo[h] Coumarin-Based Bright Two-Photon Fluorescent Probes for Cellular Bioimaging. *RSC Adv.* **2024**, *14*, 10255–10265. [CrossRef] [PubMed]
34. Hubenova, Y.; Bakalska, R.; Hubenova, E.; Mitov, M. Redox Interactions between Dye 4-(E)-1-ethyl-4-(2-(4-hydroxynaphthalen-1-yl)vinyl)quinolinium Bromide and NAD+/NADH. *Bulg. Chem. Commun.* **2018**, *50*, 68–74.
35. Parr, R.G. Density functional theory of atoms and molecules. In *Horizons of Quantum Chemistry, Proceedings of the Third International Congress of Quantum Chemistry, Kyoto, Japan, 29 October–3 November 1979*; Springer: Dordrecht, The Netherlands, 1989; pp. 5–15.
36. Mustafa, G.; Sabir, S.; Sumrra, S.H.; Zafar, W.; Arshad, M.N.; Hassan, A.U.; Akhtar, A.; Ashfaq, M.; Ashfaq, M.; Asiri, A.M. Synthesis, structure elucidation, SC-XRD/DFT, molecular modelling simulations and DNA binding studies of 3, 5-diphenyl-4, 5-dihydro-1 H-pyrazole chalcones. *J. Biomol. Struct. Dyn.* **2025**, *43*, 1831–1846. [CrossRef]
37. Hassan, A.U.; Sumrra, S.H.; Zubair, M.; Mustafa, G.; Nazar, M.F.; Zafar, M.N. Structurally modulated D-π-DA (Semiconductor) anchoring dyes to enhance the tunable NLO response: A DFT/TDDFT quest for new photovoltaic materials. *Struct. Chem.* **2023**, *34*, 1043–1060. [CrossRef]
38. Bruker AXS Inc. *APEX6*, version 2024.9-0; Bruker AXS Inc.: Madison, WI, USA, 2024.
39. Bruker AXS Inc. *SAINT*, version 8.41; Bruker AXS Inc.: Madison, WI, USA, 2016.
40. Krause, L.; Herbst-Irmer, R.; Sheldrick, G.M.; Stalke, D. SADABS: Software for Empirical Absorption Correction. *J. Appl. Cryst.* **2015**, *48*, 3–10. [CrossRef] [PubMed]
41. Sheldrick, G.M. SHELXT–Integrated Space-Group and Crystal-Structure Determination. *Acta Crystallogr. A* **2015**, *71*, 3–8. [CrossRef]
42. Sheldrick, G.M. Crystal Structure Refinement with SHELXL. *Acta Crystallogr. C* **2015**, *71*, 3–8. [CrossRef]
43. Dolomanov, O.V.; Bourhis, L.J.; Gildea, R.J.; Howard, J.A.K.; Puschmann, H. OLEX2: A Complete Structure Solution, Refinement and Analysis Program. *J. Appl. Cryst.* **2009**, *42*, 339–341. [CrossRef]
44. Macrae, C.F.; Edgington, P.R.; McCabe, P.; Pidcock, E.; Shields, G.P.; Taylor, R.; Towler, M.; van de Streek, J. Mercury: Visualization and Analysis of Crystal Structures. *J. Appl. Cryst.* **2006**, *39*, 453–457. [CrossRef]
45. Frisch, M.J.; Trucks, G.W.; Schlegel, H.B.; Scuseria, G.E.; Robb, M.A.; Cheeseman, J.R.; Scalmani, G.; Barone, V.; Mennucci, B.; Petersson, G.A.; et al. *Gaussian 09, Revision D.01*; Gaussian, Inc.: Wallingford, CT, USA, 2009.
46. Garrett, M.M.; Huey, R.; Lindstrom, W.; Sanner, M.F.; Belew, R.K.; Goodsell, D.S.; Olson, A.J. AutoDock4 and AutoDockTools4: Automated Docking with Selective Receptor Flexibility. *J. Comput. Chem.* **2009**, *30*, 2785–2791. [CrossRef]
47. Tumbarski, Y.; Lincheva, V.; Petkova, N.; Nikolova, R.; Vrancheva, R.; Ivanov, I. Antimicrobial activity of extract from aerial parts of potentilla (*Potentilla reptans* L.). *Acad. J. Ind. Technol.* **2017**, *4*, 37–43.
48. Makar, S.; Saha, T.; Singh, S.K. Naphthalene, a versatile platform in medicinal chemistry: Sky-high perspective. *Eur. J. Med. Chem.* **2019**, *161*, 252–276. [CrossRef]

49. Johnson, A. Antimicrobial Therapy and Vaccines, Volume II Antimicrobial Agents. *J. Antimicrob. Chemother.* **2006**, *57*, 801. [CrossRef]
50. Spectral Database for Organic Compounds (SDBS). Available online: http://sdbs.db.aist.go.jp/sdbs/cgi-bin/direct_frame_top.cgi (accessed on 28 May 2025).
51. Todorova, M.; Seidel, R.W.; Stoyanova, M.; Kolev, T.M.; Bakalska, R. Comparing the Crystal Structures and Spectroscopic Properties of a p-Hydroxy Styrylquinolinium Dye with Those of Its p-Dimethylamino Analogue. *Heliyon* **2024**, *10*, e29315. [CrossRef]
52. Pretsch, E.; Buhlmann, P.; Affolter, C. *Structure Determination of Organic Compounds: Tables of Spectral Data*; Springer: Berlin/Heidelberg, Germany; New York, NY, USA, 2000; ISBN 3-540-67815-8.
53. Li, Y.; Zhang, J.-X.; Fu, P.-Z.; Wu, Y.-C. 4-{2-[4-(Dimethylamino)phenyl]ethenyl}-1-methylpyridinium 2,4,6-trimethylbenzenesulfonate monohydrate. *Acta Crystallogr. Sect. E Struct. Rep. Online* **2011**, *67*, o823. [CrossRef]
54. Canakdag, M.; Feizi-Dehnayebi, M.; Kundu, S.; Sahin, D.; İlhan, İ.Ö.; Alhag, S.K.; Al-Shuraym, L.A.; Akkoc, S. Comprehensive Evaluation of Purine Analogues: Cytotoxic and Antioxidant Activities, Enzyme Inhibition, DFT Insights, and Molecular Docking Analysis. *J. Mol. Struct.* **2025**, *1323*, 140798. [CrossRef]
55. Mishra, A.K.; Behera, R.K.; Fronczek, F.; Vidyasagar, M.; Behera, G.B. X-Ray Crystallographic Study of 1-Methyl-4-(4-N,N-Dimethylamino)-Styryl Pyridinium Iodide. *Indian J. Chem. Sect. B* **1999**, *38*, 982–985.
56. Fun, H.-K.; Chanawanno, K.; Chantrapromma, S. (*E*)-2-[4-(Dimethylamino)styryl]-1-methylpyridinium triiodide. *Acta Crystallogr. Sect. E Struct. Rep. Online* **2011**, *67*, o2151. [CrossRef] [PubMed]
57. Zhou, S.; Zhang, Q.; Tian, X.; Hu, G.; Hao, F.; Wu, J.; Tian, Y. Synthesis, crystal structure, optical properties, DNA-binding and cell imaging of an organic chromophore. *Dye. Pigment.* **2011**, *92*, 689–695. [CrossRef]
58. Senthil, K.; Kalainathan, S.; Kumar, A.R. Synthesis, growth, crystal structure, spectral, thermal, mechanical and optical studies of stilbazolium derivative single crystal: 2-[2-(4-Diethylamino-phenyl)-vinyl]-1-methyl-pyridinium naphthalene-2-sulfonate (DESNS). *Spectrochim. Acta Part A Mol. Biomol. Spectrosc.* **2014**, *124*, 603–610. [CrossRef]
59. Lee, S.-H.; Jazbinsek, M.; Yun, H.; Kim, J.-T.; Lee, Y.S.; Jung, Y.M.; Lee, S.W.; Kwon, O.-P. New quinolinium polymorph with optimal packing for maximal off-diagonal nonlinear optical response. *Dye. Pigment.* **2013**, *96*, 435–439. [CrossRef]
60. Chantrapromma, S.; Jindawong, B.; Fun, H.-K.; Patil, P.S. Crystal and molecular structures of 2-[(E)-2-(4-hydroxy-3-methoxyphenyl)ethenyl]-1-methylquinolinium 4-methoxybenzenesulfonate. *Anal. Sci. X-Ray Struct. Anal. Online* **2007**, *23*, x81–x82. [CrossRef]
61. Zhang, X.H.; Wang, L.Y.; Zhai, G.H.; Wen, Z.Y.; Zhang, Z.X. X-ray and DFT studies of the structure and spectral property of 2-[2-(4-dimethylaminophenyl)ethenyl]-1-methylpyridinium iodide. *J. Mol. Struct.* **2008**, *881*, 117–122. [CrossRef]
62. LoPachin, R.M.; Gavin, T. Reactions of electrophiles with nucleophilic thiolate sites: Relevance to pathophysiological mechanisms and remediation. *Free Radic. Res.* **2016**, *50*, 195–205. [CrossRef] [PubMed] [PubMed Central]
63. Hassan, M.; Flanagan, T.W.; Kharouf, N.; Bertsch, C.; Mancino, D.; Haikel, Y. Antimicrobial Proteins: Structure, Molecular Action, and Therapeutic Potential. *Pharmaceutics* **2023**, *15*, 72. [CrossRef]
64. Ashwell, G.J.; Mohib, A. Improved molecular rectification from self-assembled monolayers of a sterically hindered dye. *J. Am. Chem. Soc.* **2005**, *127*, 16238–16244. [CrossRef]
65. Abu-Dief, A.M.; Feizi-Dehnayebi, M.; Nafady, A.; Almalki, M.A.; Kassem, A.M.; Abu Al-Ola, K.A.; Altayeb, B.M.; Abdel-Rahman, L.H. Fabrication, Structural Inspection, Stability Studies in Solution and DFT Calculations of Some Novel Complexes Derived from 4-(Benzothiazol-2-yliminomethyl)-Phenol Ligand: Pharmaceutical Applications Supported by Molecular Docking Approach. *J. Mol. Struct.* **2025**, *1328*, 141284. [CrossRef]
66. Feizi-Dehnayebi, M.; Ziarani, G.M.; Lohith, T.N.; Ghareghomi, S.; Panahande, Z.; Farsadrooh, M.; Majidinia, M. Probing the Biological Activity of Isatin Derivatives Against Human Lung Cancer A549 Cells: Cytotoxicity, CT-DNA/BSA Binding, DFT/TD-DFT, Topology, ADME-Tox, Docking and Dynamic Simulations. *J. Mol. Liq.* **2025**, *428*, 127475. [CrossRef]
67. Hemmati, R.; Abdi, A.; Feizi-Dehnayebi, M.; Farajzadeh, M.; Ziarani, G.M.; Banitalebi, A.; Badiei, A. Benzoguanamine Dimer as a Novel Fluorophore Probe for Hg^{2+} Ion Detection in *Pampus argenteus* Fish Supported by DFT Approach. *J. Environ. Chem. Eng.* **2025**, *13*, 116981. [CrossRef]
68. Rossi, A.; Stagno, C.; Piperno, A.; Iraci, N.; Panseri, S.; Montesi, M.; Feizi-Dehnayebi, M.; Bassi, G.; Di Pietro, M.L.; Micale, N. Anticancer Activity and Morphological Analysis of Pt(II) Complexes: Their DFT Approach, Docking Simulation, and ADME-Tox Profiling. *Appl. Organomet. Chem.* **2024**, *38*, e7403. [CrossRef]
69. Ahmed, S.; Rafi, U.M.; Senthil Kumar, R.; Bhat, A.R.; Berredjem, M.; Niranjan, V.; Rahiman, A.K. Theoretical, Antioxidant, Antidiabetic and In Silico Molecular Docking and Pharmacokinetics Studies of Heteroleptic Oxovanadium(IV) Complexes of Thiosemicarbazone-Based Ligands and Diclofenac. *J. Biomol. Struct. Dyn.* **2023**, *42*, 8407–8426. [CrossRef]
70. Todorova, M.; Bakalska, R.; Feizi-Dehnayebi, M.; Ziarani, G.M.; Pencheva, M.; Stojnova, K.; Milusheva, M.; Nedialkov, P.; Cherneva, E.; Kolev, T.; et al. Synthesis, Anti-Inflammatory Activity, and Docking Simulation of a Novel Styryl Quinolinium Derivative. *Appl. Sci.* **2024**, *15*, 284. [CrossRef]
71. Mohamed, A.; Dayo, M.; Alahmadi, S.; Ali, S. Anti-Inflammatory and Antimicrobial Activity of Silver Nanoparticles Green-Synthesized Using Extracts of Different Plants. *Nanomaterials* **2024**, *14*, 1383. [CrossRef]

72. Vaitkienė, S.; Kuliešienė, N.; Sakalauskaitė, S.; Bekere, L.; Krasnova, L.; Vigante, B.; Duburs, G.; Daugelavičius, R. Antifungal Activity of Styrylpyridinium Compounds against *Candida albicans*. *Chem. Biol. Drug Des.* **2021**, *97*, 253–265. [CrossRef]
73. Dinarello, C.A. Immunological and inflammatory functions of the interleukin-1 family. *Annu. Rev. Immunol.* **2009**, *27*, 519–550. [CrossRef] [PubMed]
74. Van Den Eeckhout, B.; Tavernier, J.; Gerlo, S. Interleukin-1 as Innate Mediator of T Cell Immunity. *Front. Immunol.* **2021**, *11*, 621931. [CrossRef] [PubMed]
75. Kwak, J.H.; Baek, S.H.; Woo, Y.; Han, J.K.; Kim, B.G.; Kim, O.Y.; Lee, J.H. Beneficial Immunostimulatory Effect of Short-Term Chlorella Supplementation: Enhancement of Natural Killer Cell Activity and Early Inflammatory Response (Randomized, Double-Blinded, Placebo-Controlled Trial). *Nutr. J.* **2012**, *11*, 53. [CrossRef] [PubMed]
76. Zhang, J.; Cai, K.; Mishra, R.; Jha, R. In Ovo Supplementation of Chitooligosaccharide and Chlorella Polysaccharide Affects Cecal Microbial Community, Metabolic Pathways, and Fermentation Metabolites in Broiler Chickens. *Poult. Sci.* **2020**, *99*, 4776–4785. [CrossRef]
77. Finlay, C.M.; Lavelle, E.C.; McEntee, C.P. Divergent Roles for the IL-1 Family in Inflammation and Gastrointestinal Homeostasis. *Front. Immunol.* **2019**, *10*, 1266. [CrossRef]
78. Lopez-Castejon, G.; Brough, D. Understanding the Mechanism of IL-1β Secretion. *Cytokine Growth Factor Rev.* **2011**, *22*, 189–195. [CrossRef]
79. Dinarello, C.A. A Clinical Perspective of IL-1β as the Gatekeeper of Inflammation. *Eur. J. Immunol.* **2011**, *41*, 1203–1217. [CrossRef] [PubMed]
80. Förstermann, U.; Sessa, W.C. Nitric Oxide Synthases: Regulation and Function. *Eur. Heart J.* **2012**, *33*, 829–837. [CrossRef] [PubMed]

Disclaimer/Publisher's Note: The statements, opinions and data contained in all publications are solely those of the individual author(s) and contributor(s) and not of MDPI and/or the editor(s). MDPI and/or the editor(s) disclaim responsibility for any injury to people or property resulting from any ideas, methods, instructions or products referred to in the content.